

# Observation of a Critical Charge Mode in a Strange Metal

Hisao Kobayashi,<sup>1,2\*</sup> Yui Sakaguchi,<sup>1</sup> Hayato Kitagawa,<sup>1,2</sup> Momoko Oura,<sup>1,2</sup>  
Shugo Ikeda,<sup>1,2</sup> Kentaro Kuga,<sup>3</sup> Shintaro Suzuki,<sup>3</sup> Satoru Nakatsuji,<sup>3,4,5,6\*</sup>  
Ryo Masuda,<sup>2,7</sup> Yasuhiro Kobayashi,<sup>2,7</sup> Makoto Seto,<sup>2,7</sup>  
Yoshitaka Yoda,<sup>8</sup> Kenji Tamasaku,<sup>2</sup>  
Yashar Komijani,<sup>9,10</sup> Premala Chandra,<sup>10</sup> Piers Coleman<sup>10,11\*</sup>

<sup>1</sup>Graduate School of Material Science, University of Hyogo, 3-2-1 Koto, Hyogo 678-1297, Japan

<sup>2</sup>RIKEN SPring-8 Center, Hyogo 679-5148, Japan

<sup>3</sup>Institute for Solid State Physics, University of Tokyo, Kashiwa 277-8581, Japan

<sup>4</sup>Department of Physics, University of Tokyo, Hongo, Bunkyo-ku, Tokyo 113-0033, Japan

<sup>5</sup>Trans-scale Quantum Science Institute, University of Tokyo, Bunkyo-ku, Tokyo 113-0033, Japan

<sup>6</sup>Institute for Quantum Matter and Department of Physics and Astronomy,  
Johns Hopkins University, Baltimore, Maryland 21218, USA

<sup>7</sup>Institute for Integrated Radiation and Nuclear Science, Kyoto University, Osaka 590-0494, Japan

<sup>8</sup>Japan Synchrotron Radiation Research Institute, Hyogo 679-5198, Japan

<sup>9</sup>Department of Physics, University of Cincinnati, Cincinnati, Ohio 45221-0011, USA

<sup>10</sup>Department of Physics and Astronomy, Rutgers University, Piscataway, New Jersey 08854, USA

<sup>11</sup>Hubbard Theory Consortium, Department of Physics,  
Royal Holloway, University of London, Egham, Surrey TW20 0EX, UK

\*To whom correspondence should be addressed; E-mail: kobayash@sci.u-hyogo.ac.jp,  
satoru@phys.s.u-tokyo.ac.jp, coleman@physics.rutgers.edu

February 28, 2022

Quantum electronic matter has long been understood in terms of two limiting behaviors of electrons: one of delocalized metallic states, and the other of localized magnetic states. Understanding the strange metallic behavior which develops at the brink of localization demands new probes of the underlying electronic charge dynamics. Using a state-of-the-art technique, synchrotron-radiation-based Mössbauer spectroscopy, we have studied the longitudinal charge fluctuations of the strange metal phase of  $\beta$ -YbAlB<sub>4</sub> as a function of temperature and pressure. We find that the usual single absorption peak in the Fermi-liquid regime splits into two peaks upon entering the critical regime. This spectrum is naturally interpreted as a single nuclear transition, modulated by nearby electronic valence fluctuations whose long time-scales are further enhanced, due to the formation of charged polarons. Our results represent a direct observation of critical charge fluctuations as a new signature of strange metals.

The strange metal (SM) is a ubiquitous state of matter found to develop in quantum materials with strong correlations, often appearing as a fan-shaped region of the phase diagram centered around an unstable quantum critical (QC) point. SMs share many commonalities, most-notably a logarithmic temperature ( $T$ ) dependence of specific heat  $C/T \sim -\log T$ , a linear-in- $T$  resistivity  $\rho(T) \sim T$  (1) and a strong violation of Kohlers law in the magnetotransport (2, 3, 4). These properties and their universality defy the standard concept of quasiparticle excitations and the conventional wisdom of momentum-relaxation-origin of the conductivity, central to the Fermi liquid (FL) theory of metals. This enigma has prompted a wide range of possible origins, including spin-density instability (1), Fermi surface instability (5, 6, 7), valence quantum criticality (8), charge stripes (9), and nematicity (10, 11, 12) and motivated novel approaches, including the holographic duality (13, 14, 15) and simulation using cold atoms (16).

While the spin dynamics at quantum criticality has been extensively studied, little is known experimentally about the charge dynamics as appropriate laboratory probes are scarce. Conventionally, charge dynamics are studied using optical spectroscopy (17), but these methods only probe the low-momenta, divergence-free *transverse* components of the current  $\mathbf{J} = \sigma \mathbf{E} \perp \mathbf{k}$  that, by the continuity equation, do not couple to fluctuations in the charge density. Longitudinal charge fluctuations can be probed by electron energy loss spectroscopy (EELS) but are limited to energies above the Debye energy due to a phonon background (18, 19, 20). A classic method to detect low frequency longitudinal charge dynamics is Mössbauer spectroscopy, successfully used in the past to detect the slowing of the charge dynamics at charge ordering transitions of Eu and Fe based compounds (21, 22).

However, the widespread adoption of Mössbauer methods has been long hindered by the lack of suitable radioisotope sources. To overcome these difficulties, a new generation of Mössbauer spectroscopy has recently been developed using synchrotron radiation (SR) (23). SR-based Mössbauer spectroscopy (see Fig. 1 A) can be used for a wide range of Mössbauer

isotopes, providing improved energy resolution for these isotopes with shorter-lifetimes; it offers an unprecedented capability to select a particular nuclear transition, taking advantage of the perfectly polarized SR. This new approach presents an ideal probe to resolve *longitudinal* charge dynamics in materials for which conventional Mössbauer techniques are inapplicable.

Here we report the first direct observation of critical charge dynamics in a SM regime using SR-based  $^{174}\text{Yb}$  Mössbauer spectroscopy. The heavy fermion metal  $\beta\text{-YbAlB}_4$  provides an ideal platform to study a SM regime at ambient pressure in a stoichiometric crystal (3, 24). In  $\beta\text{-YbAlB}_4$ , core level X-ray studies have established the presence of an intermediate valence state caused by valence fluctuations between two ionic configurations (25)  $\text{Yb}^{2+} \rightleftharpoons \text{Yb}^{3+} + e^-$ . Usually, in heavy fermion compounds, such valence fluctuations are too fast to be observed by Mössbauer spectroscopy (26, 27, 28, 29), but here we show that this is not the case in the SM.

Mössbauer spectroscopy measures the shift in a nuclear absorption line due to changes in the local ( $q$ -integrated) charge density. The characteristic time-scale of the measurement is the lifetime of the nuclear excited state,  $\tau_0 \sim 2.5\text{ns}$  in  $^{174}\text{Yb}$ . Charge fluctuations that are much shorter in time than  $\tau_0$  produce a single motionally narrowed absorption line, whereas charge fluctuations that are much longer in time than  $\tau_0$  produce a double peak absorption line, corresponding to the two different valence states of the Yb ion (see Figure 1 C). By fitting the Mössbauer absorption line-shape, one can detect charge fluctuations with time-scales in the range  $\sim 0.1\tau_0$  to  $\sim 10\tau_0$  (30).

$\beta\text{-YbAlB}_4$  exhibits quantum criticality without tuning in an intermediate valence state (25), and the application of an infinitesimal magnetic field  $B$  tunes the SM into a FL with  $k_{\text{B}}T_{\text{FL}} \sim \mu_{\text{B}}B$ . The slope of the linear-in- $T$  resistivity  $\rho(T) \sim T$  over  $T$  between 0.5 and 25 K at ambient pressure, corresponds to a nearly quantum-saturated scattering rate  $\tau_{\text{tr}}^{-1} = 0.4 \times k_{\text{B}}T/\hbar$  (30), thus establishing  $\beta\text{-YbAlB}_4$  as a system with Planckian dissipation (31). This anomalous  $\rho(T)$  and its extension over a broad pressure ( $p$ ) range from ambient pressure to  $p^* \sim 0.5\text{GPa}$

(3, 24, 32) (see Fig. 1 B) provides an excellent setting for high precision measurements of the critical charge fluctuations, likely of relevance to the broader family of SMs.

We have investigated how the QC behavior in the SM regime affects the charge dynamics, following their evolution as the SM regime at ambient pressure transforms into a FL regime under pressure. Above 9K at ambient pressure (Fig. 2 A) the Mössbauer spectra exhibit a single line feature. However, below  $T^* \sim 10\text{K}$ , as one enters the QC region, this peak broadens into a two-peak structure, with  $5\sigma$  significance (30). Fig. 2 B shows how this two-peak structure observed for  $p < 0.7\text{GPa}$  at 2K coalesces into a single peak around  $p \sim 1.2\text{GPa}$ , ultimately sharpening into an almost resolution-limited peak at  $p = 2.3\text{GPa}$  characteristic of a Fermi liquid (30).

The local symmetry at the Yb site of  $\beta\text{-YbAlB}_4$  with the orthorhombic structure allows us to rule out a nuclear origin of the double-peak structure. For  $c \parallel \mathbf{k}_0$  (the propagation vector of the incident X-ray), the symmetry selects two degenerate nuclear transitions  $I_g = 0 \rightarrow I_e^z = \pm 1$  from the five  $E2$  nuclear transitions ( $\Delta I^z = 0, \pm 1$ , and  $\pm 2$ ) of the  $^{174}\text{Yb}$  Mössbauer resonance (33) (see Figs. 1 A and C). The absence of magnetic order in  $\beta\text{-YbAlB}_4$  (24, 32) also eliminates magnetic and non-axially symmetric quadrupolar hyperfine interactions as explanations (30). This leaves a combination of the electric monopole and axially symmetric quadrupolar interactions, linking the hyperfine energy to the valence state of the rare-earth ion, as the only candidate for the observed splitting. The presence of a Mössbauer line splitting then implies a distribution of Yb valences within the crystal. We now argue that these result from slow dynamic charge fluctuations.

All Yb sites are crystallographically equivalent in  $\beta\text{-YbAlB}_4$  and SR X-ray diffraction measurements (34) show that the lattice structure does not change up to 3.5GPa at 7K; furthermore the absence of any low-temperature phase transitions rules out the possibility of a charge density wave (30). Moreover, the residual resistivity ratio (RRR) exceeds 100, indicating the low

levels of quenched disorder in this material. Since disorder broadens the Mössbauer absorption peak, our ability to resolve the double-peak structure is consistent with this conclusion. An attempt to fit the Mössbauer spectrum with two nuclear transitions (i.e. a static hyperfine interaction), using a width corresponding to the experimental energy resolution, fails to reconstruct the feature at 2K and  $\sim 0$  mm/s (blue broken line). Thus the two-peak structure and line broadening observed for  $T < 5$ K and  $p < 0.7$ GPa must derive from a single nuclear transition that is dynamically modulated by fluctuations between two different Yb charge states (i.e. a time-dependent hyperfine interactions) (Fig. 1 C) (30).

We have analyzed our Mössbauer spectra at ambient pressure using a stochastic theory (35, 36, 37) with a single nuclear transition modulated by two different charge states (30). Fig. 2 A shows that the predicted spectra (red lines) well reproduce the two-peak structure in the spectra at low  $T$ s and its subsequent collapse into a single line with increasing  $T$ .

At ambient pressure, the extracted fluctuation time  $\tau_f$  between two different Yb charge states is unusually long compared to the electronic timescales, exhibiting a slow power-law growth  $T^{-\eta}$  ( $\eta \sim 0.2$ ) on cooling below  $T^*$  (Fig. 2 C). The energy difference between two selected nuclear transitions is almost independent of  $T$  up to 20K (30), so that the development of the two-peak structure in the observed spectra must derive from the marked low- $T$  growth in  $\tau_f$ . On the other hand, as shown in Fig. 2 B, the gradual collapse of the two-peak structure in the observed  $^{174}\text{Yb}$  Mössbauer spectra at 2K with increasing  $p$  indicates that fluctuation timescale  $\tau_f$  becomes shorter as a function of  $p$ . The spectra at  $p < 1.2$ GPa can only be analyzed and reconstructed by the same stochastic model used at the ambient pressure, while the spectrum observed at 2.3GPa was simply fit using the static model. The line-width of this single absorption component was found to be  $\Gamma = 1.11$  mm/s, slightly broader than the resolution limit  $\Gamma_0 = \hbar/\tau_0 = 1.00$  mm/s (3mK), for  $^{174}\text{Yb}$  Mössbauer spectroscopy ( $\tau_0 = 2.58$ ns).

As seen in Fig. 2 D,  $\tau_f$  gradually decreases with increasing  $p$ , exhibiting a kink across  $\sim p^*$

in between 0.5 and 1GPa, approaching the resolution limit at 2.3GPa. This is roughly consistent with previous  $\rho(T)$  measurements in  $\beta$ -YbAlB<sub>4</sub> (32); at  $T < 0.5\text{K}$  and under  $p$ ,  $\rho(T)$  displays  $\rho \sim T^\alpha$  with  $\alpha = 3/2$  below  $p^*$  and further application of pressure increases the exponent to  $\alpha = 2$ , stabilizing a FL state at about 1GPa (32).

The above consistency leads us to interpret the split line-shape observed in the Mössbauer spectra of the SM as unusually slow valence fluctuations between the Yb<sup>2+</sup> and Yb<sup>3+</sup> ionic-like states in  $\beta$ -YbAlB<sub>4</sub>, on a timescale  $\tau_f > 1\text{ns}$  that follows an approximate power-law growth  $\tau_f \sim T^{-0.2}$  with decreasing temperature below  $T^*$ . The Yb<sup>3+</sup> ground state is a  $J_z = \pm 5/2$  moment as deduced by varying incident angle of the X-ray (30). The slow charge fluctuations extend up to  $p^*$ , beyond which a conventional valence fluctuation state with rapid charge fluctuation takes over in the pressured regime corresponding to the FL regime.

The unusual aspect of the observed charge dynamics is that not only are they slower than the Planckian time  $\tau_f \gg \tau_{tr} \sim 10^{-2}\text{ns}$  at 2K, but they are also slower than the characteristic time-scale of the lattice vibrations as we will show shortly. In this situation, the lattice is expected to adiabatically respond to the associated charge redistribution. Each valence fluctuation of Yb atoms is then dressed by  $N_p$  phonons, leading to the formation of a polaron (38, 39) and renormalizing the matrix element for the charge fluctuations and providing a mechanism for enhancing their time-scale ( $\tau_f \rightarrow \tau_f e^{N_p}$ ) (30). Analysis of the Mössbauer spectra allows us to directly check this scenario. We have used the  $T$ -dependence of the absorption components in the spectra to determine the Lamb-Mössbauer (recoil-free) factor  $f_{LM}$  in  $\beta$ -YbAlB<sub>4</sub>, the equivalent of the Debye-Waller factor in a usual scattering experiment. Generally,  $-\ln(f_{LM}) = k_0^2 \langle \Delta z^2 \rangle$ , where  $\Delta z$  is an atomic displacement from a regular position in a crystal along the direction of  $\mathbf{k}_0$  (40). The expression for the variance in atomic position is

$$\langle \Delta z^2 \rangle \propto \int_0^\infty d\omega \frac{F(\omega)}{\omega} \overbrace{\left[ \frac{1}{2} + \frac{1}{e^{\omega/T} - 1} \right]}^{\frac{1}{2} \coth(\beta\omega/2)} \quad (1)$$

where  $F(\omega)$  is the (partial) phonon density of states. In a Debye model,  $F(\omega) \propto \omega^2$  which leads to  $\langle \Delta z^2 \rangle \propto [3/2 + (\pi/\Theta_D)^2 T^2]$  at  $T \ll \Theta_D$ , where  $\Theta_D$  is the Debye temperature (30). As seen in Fig. 3 A, this Debye relation holds above  $T^*$  at ambient pressure, where  $\tau_f$  ( $\sim 1.15$ ns) is independent of  $T$ ; from this we estimate  $\Theta_D = 95$ K, corresponding to the lattice response time  $\tau_L \sim h/k_B \Theta_D \sim 0.5$ ps, so that  $\tau_f \gg \tau_L$ . The estimated  $\Theta_D$  ( $= 95$ K) value is unusually smaller than that (195K) of a conventional valence fluctuation metal  $\text{YbAl}_2$  (41). This indicates that the lattice vibrations are soft in  $\beta$ - $\text{YbAlB}_4$ , suggesting an enhanced effective coupling between slow charge fluctuation modes and lattice vibrations.

Additionally, we see from Fig. 3A that in the QC regime below  $T^*$ , where  $\tau_f$  develops temperature-dependence,  $\langle \Delta z^2 \rangle$  departs from this Debye behavior, indicating an enhancement in the quantum fluctuations,  $\langle \Delta z^2 \rangle = \langle \Delta z^2 \rangle_{\text{Debye}} + \delta \langle \Delta z^2 \rangle$ , of the Yb ions. Notably, the  $\sqrt{\delta \langle \Delta z^2 \rangle} \sim 0.014 \text{\AA}$  rms fluctuation observed here is comparable to the quantum fluctuations of the phonon mode, around  $0.05 \text{\AA}$  estimated from  $\frac{1}{4} k_B \Theta_D \sim \frac{1}{2} m_{\text{Yb}} (k_B \Theta_D / \hbar)^2 \langle \Delta z^2 \rangle$ . Fig. 3 B shows that  $\langle \Delta z^2 \rangle$  is approximately constant at 2K for  $p < p^*$  and then drops when  $p > p^*$ , indicating that the anomalous vibrations of the lattice,  $\delta \langle \Delta z^2 \rangle$ , disappear in the FL regime at low temperatures.

The saturation of  $\langle \Delta z^2 \rangle$  for  $T < T^*$  and  $p < p^*$  implies that the phonon spectrum  $F(\omega)$  has changed its form to compensate the  $\coth(\beta\omega/2)$  term in the integral (1). This then suggests that at energies and temperatures below  $T^*$ ,  $F(\omega)$  acquires a temperature-dependence  $F(\omega, T) = \phi(\omega) \tanh(\omega/2T)$  that cancels the  $\coth(\omega/2T)$  term in integral (1). The function  $\tanh(\omega/2T) \sim \omega/2T$  for  $\omega \ll T$  and  $\tanh(\omega/2T) \sim 1$  for  $\omega \gg T$ , and thus has the Marginal Fermi Liquid (MFL) form. This enhancement in phonon density of states should be observable in inelastic neutron scattering measurements. Since the phonons are linearly coupled to the charge density of the electrons, the appearance of a MFL component in the phonon spectrum is an indication of MFL behavior in the charge fluctuations. The enhancement of  $\tau_f$  by polaron



formation has been crucial for slowing the charge fluctuations down to time-scales accessible to Mössbauer spectroscopy.

A possible interpretation of our results is the quantum critical tuning of a critical end point of a classical valence transition (42) between the  $\text{Yb}^{2+}$  and  $\text{Yb}^{3+}$  ionic states. Such first order valence transition lines, with second order end-points, are well established in rare earth compounds. It has been suggested (42) that the tuning of such an endpoint to zero temperature may provide an explanation of the observed Mössbauer spectra.

An alternative interpretation is that the observed valence fluctuation modes are an intrinsic property of the SM regime connected with a spin charge separation that develops with the collapse of the  $f$ -electron Fermi surface (43, 44, 45, 46). This scenario suggests that similar slow charge fluctuations will be manifested in the Mössbauer spectra of any partial Mott localization critical point, e.g. in other heavy-fermions and Iron-based superconductors.

In summary we have provided direct evidence for unusually slow charge fluctuations in the SM regime of  $\beta\text{-YbAlB}_4$  using a state-of-the-art technique, SR-based Mössbauer spectroscopy. Because their time-scales are longer than that of the lattice response, we have inferred polaronic formation in the mixed valence regime (38, 39). Both the slow charge fluctuation modes and the anomalous vibrations of the lattice disappear in the pressure-induced FL regime. An interesting possibility is that these observed slow charge modes are the origin of the linear resistivity often observed in SMs. Various theoretical approaches (13, 14) have suggested that the novel transport properties of SMs are linked to the universal quantum hydrodynamics of a Planckian metal. Since the local equilibrium is established at the scale of Planckian time, it is natural to regard the slow charge fluctuations detected here as a possible signature of a new hydrodynamic mode. This would lead us to expect that nano-second charge fluctuations and anomalous vibrations are not unique to  $\beta\text{-YbAlB}_4$ , but rather, are universal properties of SM regimes in quantum materials.

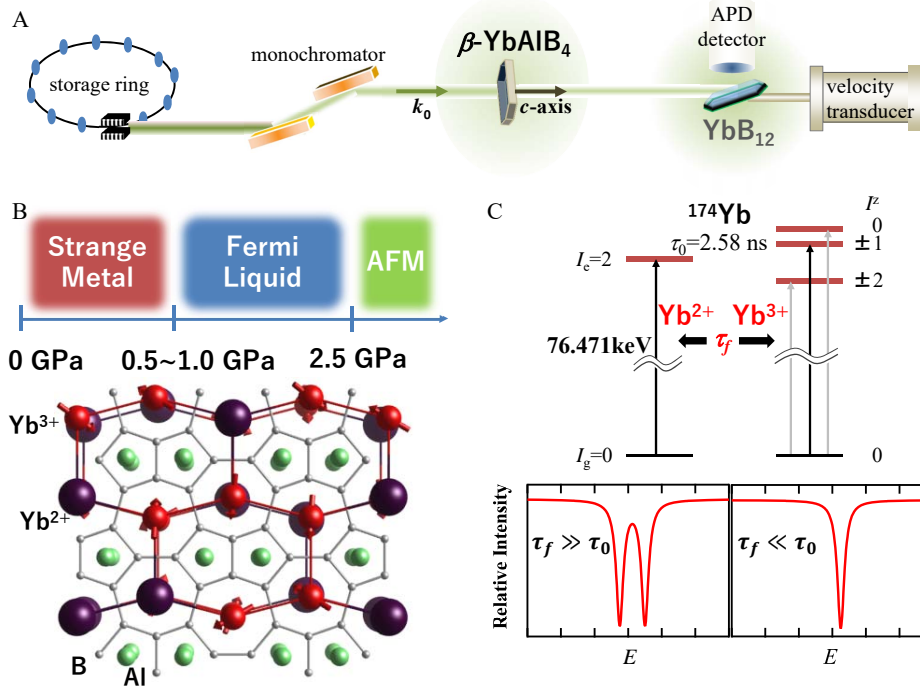


Figure 1: (A) Schematic of our experimental setup for the synchrotron-radiation-based  $^{174}\text{Yb}$  Mössbauer spectroscopy (47). The  $^{174}\text{Yb}$  nuclear resonance ( $E_\gamma = 76.471\text{keV}$ ) was obtained by synchrotron radiation using a monochromator. The  $c$ -axis of the single crystalline  $\beta$ -YbAlB<sub>4</sub> samples was aligned along the propagation vector  $\mathbf{k}_0$  of the incident X-ray under both ambient and external pressure. The single-crystalline YbB<sub>12</sub> were cooled at 26K. A Si avalanche photodiode (APD) detector was used to measure delayed incoherent emission from  $^{174}\text{Yb}$  nuclei in the YbB<sub>12</sub>. (B) Schematic phase diagram of  $\beta$ -YbAlB<sub>4</sub> as a function of pressure at low temperatures (Top) and cartoon of the crystal structure of  $\beta$ -YbAlB<sub>4</sub> with a snapshot of the Yb valences, i.e., Yb<sup>2+</sup> (large blue sphere) and Yb<sup>3+</sup> (small red sphere with arrow indicating magnetic moment) (Bottom). (C) (Top) Energy level diagrams of the excited  $^{174}\text{Yb}$  ( $I_e=2$ ) nuclear state with the lifetime of  $\tau_0 = 2.58\text{ns}$  surrounded by different charge configurations. The allowed Mössbauer transitions are indicated by arrows, where the black arrows represent two selected transitions for  $c \parallel \mathbf{k}_0$ . (Bottom) Two typical Mössbauer absorption spectra at limiting cases with  $\tau_f \gg \tau_0$  and  $\tau_f \ll \tau_0$  where  $\tau_f$  is a characteristic timescale of fluctuation between two different charge configurations.

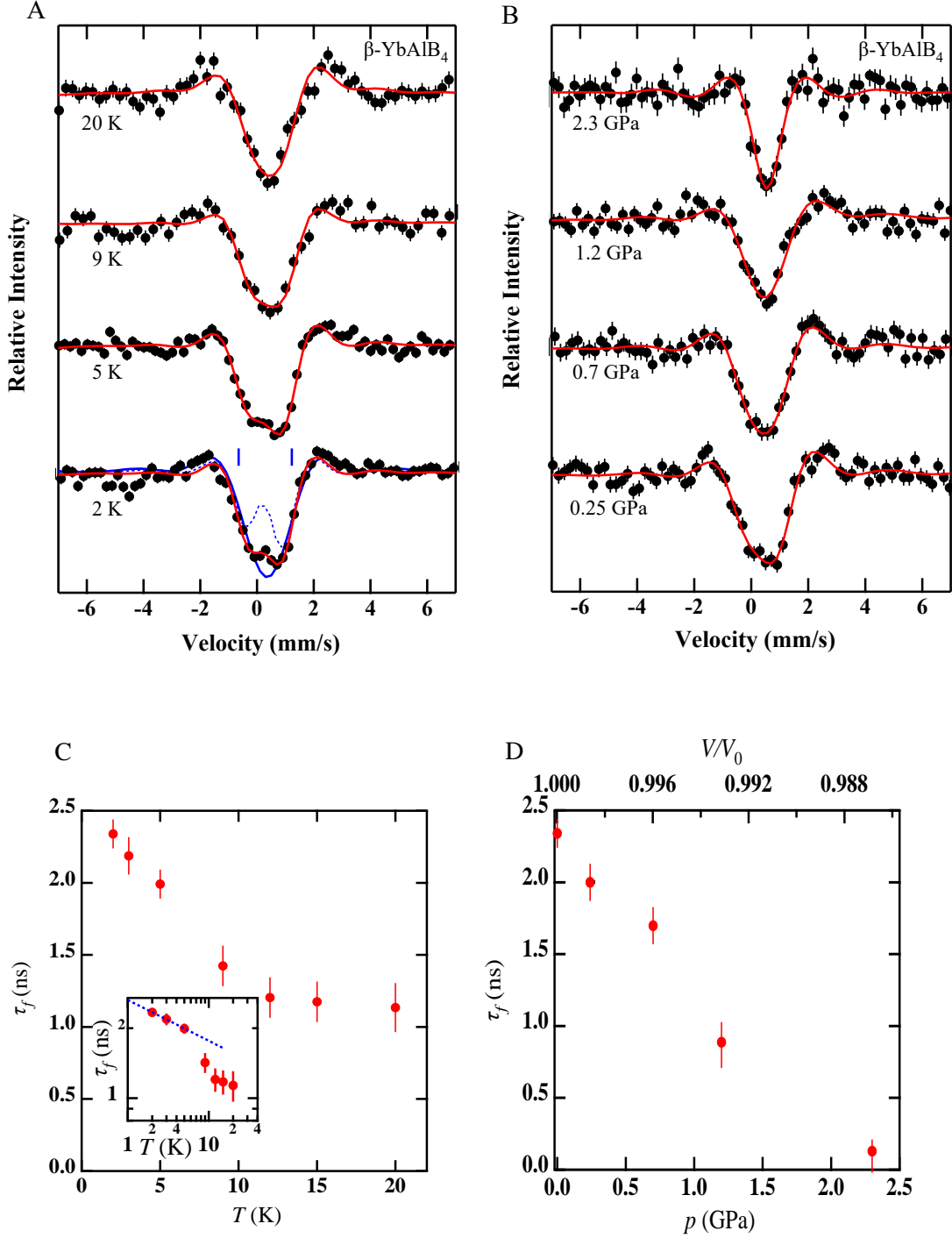


Figure 2: Selected synchrotron-radiation-based  $^{174}\text{Yb}$  Mössbauer spectra of  $\beta$ -YbAlB<sub>4</sub> as a function of temperature ( $T$ ) at ambient pressure (A) and under external pressure ( $p$ ) at 2K (B). The  $c$ -axis of the single crystalline  $\beta$ -YbAlB<sub>4</sub> samples was aligned along the propagation vector  $\mathbf{k}_0$  of the incident X-ray. The solid circles with error bar and the red solid lines present the observed and the analytical spectra, respectively. In A, the broken blue line in the spectrum at 2K represents the spectrum with two static nuclear transitions expected with our experimental energy resolution, whereas the solid blue line shows a fit to the wings of the lineshape, discarding the double-peak structure in the center. The deviation at the center corresponds to  $5\sigma$  statistical significance (30). Temperature  $T$  (C) and pressure  $p$  (D) dependences of the refined fluctuation time  $\tau_f$  between two different Yb charge states in  $\beta$ -YbAlB<sub>4</sub>. (Inset in (C)) Log-log plots of  $\tau_f$  versus  $T$  in  $\beta$ -YbAlB<sub>4</sub>. The broken line represents a  $\tau_f \sim T^{-0.2}$  relation.

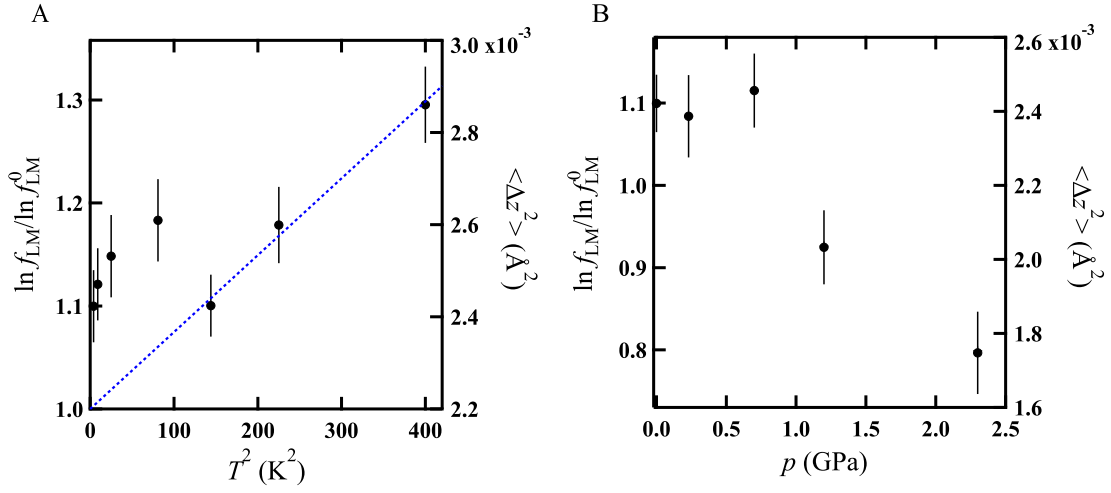


Figure 3: Lamb-Mössbauer factor  $f_{\text{LM}}$  ( $\ln f_{\text{LM}} / \ln f_{\text{LM}}^0$ ) as a function of  $T^2$  at ambient pressure (A) and under external pressure  $p$  at 2K (B) for  $\beta$ -YbAlB<sub>4</sub>. In (A), the broken line represents a linear relation between  $\ln f_{\text{LM}}$  and  $T^2$ . In (A) and (B),  $\ln f_{\text{LM}}^0$  ( $\propto -\frac{3}{2} \frac{E_{\text{R}}}{k_{\text{B}} \Theta_{\text{D}}^{\text{Yb}}}$ ) was estimated above 12K at ambient pressure. For <sup>174</sup>Yb Mössbauer resonance of  $k_0=38.75 \text{\AA}^{-1}$ ,  $\langle \Delta z^2 \rangle$  for the Yb ions was evaluated in  $\beta$ -YbAlB<sub>4</sub> from the  $T$  and  $p$  dependences of  $\ln f_{\text{LM}} / \ln f_{\text{LM}}^0$  using  $\Theta_{\text{D}}^{\text{Yb}}=95\text{K}$ . In (A) and (B), the  $\langle \Delta z^2 \rangle$  values (right axis) are  $\sim 2.6 \times 10^{-3} \text{\AA}^2$  in the SM regime and decrease to  $1.7 \times 10^{-3} \text{\AA}^2$  in the pressured regime corresponding to the FL regime, which is comparable with that for YbAl<sub>2</sub> (41).

## References and Notes

1. G. R. Stewart, *Rev. Mod. Phys.* **73**, 797 (2001).
2. T. R. Chien, Z. Z. Wang, N. P. Ong, *Phys. Rev. Lett.* **67**, 2088 (1991).
3. S. Nakatsuji, *et al.*, *Nature Physics* **4**, 603 (2008).
4. J. G. Analytis, *et al.*, *Nature Physics* **10**, 194 (2014).
5. S. Paschen, *et al.*, *Nature* **432**, 881 (2004).
6. H. Shishido, R. Settai, H. Harima, Y. Ōnuki, *J. Phys. Soc. Jpn.* **74**, 1103 (2005).
7. P. Gegenwart, Q. Si, F. Steglich, *Nature Phys.* **4**, 186 (2008).
8. K. Kuga, *et al.*, *Sci. Adv.* **4**, eaao3547 (2018).
9. F. Laliberté, *et al.*, *Nature Communications* **2**, 432 (2011).
10. E. Fradkin, S. A. Kivelson, M. J. Lawler, J. P. Eisenstein, A. P. Mackenzie, *Annual Review of Condensed Matter Physics* **1**, 153 (2010).
11. J.-H. Chu, *et al.*, *Science* **329**, 824 (2010).
12. M. Lawler, *et al.*, *Nature* **466**, 347,351 (2010).
13. J. Zaanen, Y.-W. Sun, Y. Liu, K. Schalm, *Holographic Duality in Condensed Matter Physics* (Cambridge University Press, 2016).
14. S. A. Hartnoll, A. Lucas, S. Sachdev, *Holographic Quantum Matter* (MIT Press, 2018).
15. S. A. Hartnoll, A. P. Mackenzie, *ArXiv:2107.07802* (2021).
16. P. T. Brown, *et al.*, *Science* **363**, 379 (2019).

17. L. Prochaska, *et al.*, *arxiv: 1808.02296 (2018)*. (2018).
18. S. Vig, *et al.*, *SciPost* **3**, 026 (2017).
19. M. Mitrano, *et al.*, *Proc Natl Acad Sci USA* **115**, 5392 (2018).
20. A. A. Husain, *et al.*, *Physical Review X* **9**, 041062 (2019).
21. O. Berkooz, M. Malamud, S. Shtrikman, *Solid State Communications* **6**, 185 (1968).
22. M. Takano, N. Nakanishi, Y. Takeda, S. Naka, *J. Phys. Colloques* **40**, C2 (1979).
23. M. Seto, *et al.*, *Phys. Rev. Lett.* **102**, 217602 (2009).
24. Y. Matsumoto, *et al.*, *Science* **331**, 316 (2011).
25. M. Okawa, *et al.*, *Phys. Rev. Lett.* **104**, 247201 (2010).
26. C. M. Varma, *Rev. Mod. Phys.* **48**, 219 (1976).
27. E. V. Sampathkumaran, *Hyperfine Interactions* **27**, 183 (1986).
28. R. L. Cohen, M. Eibschütz, K. W. West, *Phys. Rev. Lett.* **24**, 383 (1970).
29. I. Nowik, *Hyperfine interactions* **13**, 89 (1983).
30. *Supplementary material is available on Science online* .
31. A. Legros, *et al.*, *Nature Physics* **15**, 142 (2019).
32. T. Tomita, K. Kuga, Y. Uwatoko, P. Coleman, S. Nakatsuji, *Science* **349**, 506 (2015).
33. J. P. Hannon, G. T. Trammell, M. Blume, D. Gibbs, *Phys. Rev. Lett.* **61**, 1245 (1988).
34. Y. Sakaguchi, *et al.*, *J. Phys. Soc. Jpn.* **85**, 023602 (2016).

35. P. W. Anderson, *J. Phys. Soc. Japan* **9**, 316 (1954).
36. R. Kubo, *J. Phys. Soc. Japan* **9**, 935 (1954).
37. M. Blume, *Phys. Rev.* **174**, 351 (1968).
38. D. Sherrington, P. Riseborough, *J. Phys. Colloques* **37**, C4 (1976).
39. A. C. Hewson, D. M. Newns, *Journal of Physics C: Solid State Physics* **12**, 1665 (1979).
40. G. T. Trammell, *Phys. Rev.* **126**, 1045 (1962).
41. D. Weschenfelder, *et al.*, *Hyperfine Interactions* **16**, 743 (1983).
42. S. Watanabe, K. Miyake, *Phys. Rev. Lett.* **105**, 186403 (2010).
43. M. Oshikawa, *Phys. Rev. Lett.* **84**, 3370 (2000).
44. T. Senthil, S. Sachdev, M. Vojta, *Phys. Rev. Lett.* **90**, 216403 (2003).
45. J. H. Pixley, S. Kirchner, K. Ingersent, Q. Si, *Phys. Rev. Lett.* **109**, 086403 (2012).
46. Y. Komijani, P. Coleman, *Phys. Rev. Lett.* **122**, 217001 (2019).
47. R. Masuda, *et al.*, *Appl. Phys. Lett.* **104**, 082411 (2014).

We would like to thank M. Takigawa for very useful discussions and F. Iga for preparation of single-crystalline YbB<sub>12</sub>. The SR-based <sup>174</sup>Yb Mössbauer experiments were performed at BL09XU and BL19LXU on SPring-8 with the approval of the Japan Synchrotron Radiation Research Institute (JASRI) (Proposal Nos. 2011A1450, 2012B1521, 2013B1393, 2015A1458, 2016A1363, and 2019B1597) and RIKEN (Proposal Nos. 2016110, 20170019, 20180019, and 20190025). This work is partially supported by Grants-in-Aids for Scientific Research on Innovative Areas (15H05882 and 15H05883) from the Ministry of Education, Culture, Sports,

Science, and Technology of Japan, by CREST (JPMJCR18T3), Japan Science and Technology Agency, and by Grants-in-Aid for Scientific Research (15K05182, 16H02209, 16H06345, 19H00650, and 23102723) from the Japanese Society for the Promotion of Science (JSPS), by the Canadian Institute for Advanced Research, the National Science Foundation grant DMR-1830707 (P. Coleman and Y. K) and by the U. S. Department of Energy (DOE), Office of Science, Basic Energy Sciences under award DE-SC0020353 (P. Chandra). The Institute for Quantum Matter, an Energy Frontier Research Center was funded by DOE, Office of Science, Basic Energy Sciences under Award # DE-SC0019331. P. Chandra and P. Coleman thank S. Nakatsuji and the Institute for Solid State Physics (Tokyo) for hospitality when early stages of this work were underway. P.C., P.C. and Y.K. acknowledge the Aspen Center for Physics and NSF Grant No. PHY-1607611 where this work was discussed and further developed.



# Supplementary Materials for Observation of a Critical Charge Mode in a Strange Metal

Hisao Kobayashi,<sup>1,2\*</sup> Yui Sakaguchi,<sup>1</sup> Hayato Kitagawa,<sup>1,2</sup> Momoko Oura,<sup>1,2</sup>  
Shugo Ikeda,<sup>1,2</sup> Kentaro Kuga,<sup>3</sup> Shintaro Suzuki,<sup>3</sup> Satoru Nakatsuji,<sup>3,4,5,6\*</sup>  
Ryo Masuda,<sup>2,7</sup> Yasuhiro Kobayashi,<sup>2,7</sup> Makoto Seto,<sup>2,7</sup>  
Yoshitaka Yoda,<sup>8</sup> Kenji Tamasaku,<sup>2</sup>  
Yashar Komijani,<sup>9,10</sup> Premala Chandra,<sup>10</sup> Piers Coleman<sup>10,11\*</sup>

<sup>1</sup>Graduate School of Material Science, University of Hyogo, 3-2-1 Koto, Hyogo 678-1297, Japan

<sup>2</sup>RIKEN SPring-8 Center, Hyogo 679-5148, Japan

<sup>3</sup>Institute for Solid State Physics, University of Tokyo, Kashiwa 277-8581, Japan

<sup>4</sup>Department of Physics, University of Tokyo, Hongo, Bunkyo-ku, Tokyo 113-0033, Japan

<sup>5</sup>CREST, Japan Science and Technology Agency, Kawaguchi, Saitama 332-0012, Japan

<sup>6</sup>Institute for Quantum Matter and Department of Physics and Astronomy,

Johns Hopkins University, Baltimore, Maryland 21218, USA

<sup>7</sup>Institute for Integrated Radiation and Nuclear Science, Kyoto University, Osaka 590-0494, Japan

<sup>8</sup>Japan Synchrotron Radiation Research Institute, Hyogo 679-5198, Japan

<sup>9</sup>Department of Physics, University of Cincinnati, Cincinnati, Ohio 45221-0011, USA

<sup>10</sup>Department of Physics and Astronomy, Rutgers University, Piscataway, New Jersey 08854, USA

<sup>11</sup>Hubbard Theory Consortium, Department of Physics,

Royal Holloway, University of London, Egham, Surrey TW20 0EX, UK

\*To whom correspondence should be addressed; E-mail: kobayash@sci.u-hyogo.ac.jp,  
satoru@phys.s.u-tokyo.ac.jp, coleman@physics.rutgers.edu

February 28, 2022

# Contents

<b>A</b>	<b>Mössbauer Spectroscopy</b>	<b>3</b>
A.1	Mössbauer Spectrum: A Conceptual Discussion . . . . .	3
A.2	Importance in Studies of Heavy Electron Materials . . . . .	4
A.3	Synchrotron-radiation (SR)-based $^{174}\text{Yb}$ Mössbauer spectroscopy . . . . .	5
A.4	Oscillatory Effects of the Finite-Time Window . . . . .	6
<b>B</b>	<b>SR-based <math>^{174}\text{Yb}</math> Mössbauer Spectroscopy of Single Crystal <math>\beta\text{-YbAlB}_4</math></b>	<b>9</b>
B.1	Experimental Specifics . . . . .	9
B.2	Mössbauer Absorption Line-Shapes . . . . .	10
B.3	Spectral Fits and $^{174}\text{Yb}$ Hyperfine Hnteractions in $\beta\text{-YbAlB}_4$ . . . . .	12
B.4	Statistical Analysis of the Spectra . . . . .	17
B.5	Lamb-Mössbauer factor on $^{174}\text{Yb}$ nuclei in $\beta\text{-YbAlB}_4$ . . . . .	20
<b>C</b>	<b>Reproducibility after Thermal Cycling</b>	<b>21</b>
<b>D</b>	<b>Recent Characterization of Samples using Bulk Probes</b>	<b>22</b>
<b>E</b>	<b>Excluded Possibilities for Observed Results</b>	<b>22</b>
<b>F</b>	<b>Planckian Dissipation in <math>\beta\text{-YbAlB}_4</math></b>	<b>27</b>
<b>G</b>	<b>Supporting Theoretical Discussion</b>	<b>28</b>
G.1	Kondo Breakdown . . . . .	28
G.2	Phonons and Polarons . . . . .	30

# A Mössbauer Spectroscopy

## A.1 Mössbauer Spectrum: A Conceptual Discussion

Mössbauer spectroscopy averages the environment of the nucleus over time-scales of order a nanosecond, the lifetime of the nuclear excited state. In our experiments, quantum fluctuations in the charge of the f-electrons couple capacitively to the  $^{174}\text{Yb}$  nucleus, perturbing the nuclear excitation energies. Provided the time-scale of these charge fluctuations are slower or comparable to a nanosecond, they modify the line-shape of a nuclear transition.

The nuclear transition  $|i\rangle \rightarrow |f\rangle$  can be treated as a two-level system with transition energy  $E_f - E_i = \hbar\omega_0$ . The classic theory of lineshape broadening was developed by Anderson, Kubo and Blume (1, 2, 3, 4), before the advent of modern many-body theory. Their theory can be reformulated in a modern context (5), treating two level nuclear system as a single fermion with Hamiltonian  $H_0 = \hbar\omega_0 d^\dagger d$ . The energy shift of the nuclear energy level is then described by adding in an interaction  $H_I = \alpha n_f d^\dagger d$ , where  $\alpha$  is the monopole-like coupling to the occupancy  $\hat{n}_f$  of the f-orbitals. Thus a static valence change of the f-state produces an energy shift  $\alpha$  in the Mössbauer absorption line. With this formulation, the change in the Mössbauer absorption line-shape (Fig. A.1) can be described in terms of the self-energy  $\Sigma_d(\omega)$  of the d-fermion.

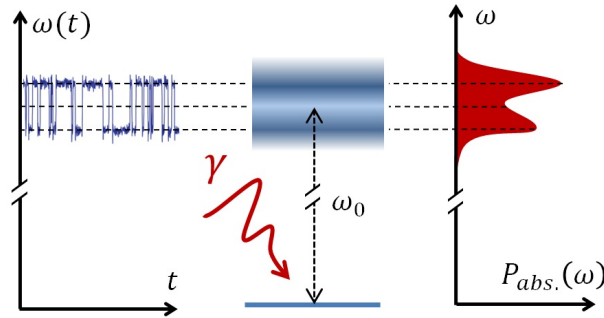


Figure A.1: Charge fluctuation in the environment capacitively couple to a two-level system (e.g. a nuclear transition) and fluctuate its resonance frequency in time. An absorption spectroscopy on this two-level leads to a modified lineshape  $P(\omega)$  which provide information about the charge fluctuation spectrum  $\chi''(\omega)/\omega$ .

The absorption cross-section (5) at a Doppler shift energy  $\hbar\omega$ ,  $P(\omega + \omega_0)$  is then related to the Green's function of the d-fermion  $G_d(\omega) = (\omega - \Sigma_d(\omega))^{-1}$  via

$$P(\omega + \omega_0) \propto \text{Im}G_d(\omega - i\eta) = \frac{\Sigma_d''}{(\omega - \Sigma_d')^2 + \Sigma_d''^2}. \quad (1)$$

To leading order in perturbation theory,

$$\Sigma_d''(\omega) = \frac{\alpha^2 T}{\omega} \chi_\rho''(\omega), \quad (2)$$

where  $\chi_\rho''(\omega)$  is the dynamical charge susceptibility of the f-state at frequency  $\omega$ . In this way, Mössbauer spectroscopy provides a direct probe of low-frequency valence fluctuations.

The energy shift  $\alpha \sim \hbar/\tau$  sets the characteristic averaging time-scale  $\tau \sim 1\text{ns}$  over which Mössbauer probes the surrounding charge fluctuations. If  $\chi''(\omega)/\omega$  is described by a Lorentzian of width  $\Lambda_{vf}$ , then the resulting power-spectrum develops a two peaked structure provided the charge fluctuation rate  $\Gamma_{vf} \ll \alpha$  is smaller than  $\alpha$ , but develops a single peak-structure when  $\Gamma_{vf} \gg \alpha$  is much faster than the isomer shift  $\alpha$ .

## A.2 Importance in Studies of Heavy Electron Materials

In heavy electron materials like  $\beta\text{-YbAlB}_4$ , charge fluctuations are known to lead to valence fluctuations (6, 7). Here strong Coulomb repulsion within the f orbitals restricts the partially filled f-shell occupancies to two orbital configurations, which in  $\beta\text{-YbAlB}_4$  are the  $4f^{13}(\text{Yb}^{3+})$  and  $4f^{14}(\text{Yb}^{2+})$ . Hybridization with the conduction sea then causes valence fluctuations,  $\text{Yb}^{2+} \rightleftharpoons \text{Yb}^{3+} + e^-$ . The simultaneous coexistence of these hybridized configurations was first established by core-level X-ray spectroscopy; the strength of the separate absorption spectra of the two instantaneous configurations gives an average Yb valence of about 2.7 in  $\beta\text{-YbAlB}_4$  (8). A series of classic experiments in the late 1970s searched carefully for the corresponding two valence configurations in Mössbauer studies (9, 10), but they were never seen. Unlike static mixed valence known in chemistry (eg in iron oxide), the quantum mechanical

valence fluctuations of a heavy fermion system are homogeneous, corresponding to hybridization energy scales of 10 – 1000K that are too fast to be observed by Mössbauer spectroscopy; usually the observed isomer shift is a single absorption feature, centered around the average of the two valences. This is what makes the new observations so fascinating, for the line-splitting that develops, without a phase transition, at low temperatures appears to correspond to a slow-down of dynamic valence fluctuations to the point where they become visible in the Mössbauer spectroscopy.

### A.3 Synchrotron-radiation (SR)-based $^{174}\text{Yb}$ Mössbauer spectroscopy

The synchrotron-radiation-(SR)-based Mössbauer spectroscopy is a new state-of-the-art experimental technique to investigate electronic states of Mössbauer atoms in compounds (*11, 12*). Figure A.2(A) shows the experimental setup for the SR-based  $^{174}\text{Yb}$  ( $E_\gamma = 76.471\text{keV}$  between the  $I_g = 0$  and  $I_e = 2$  nuclear states) Mössbauer spectroscopy at BL09XU and BL19LXU beamlines on SPring-8 (*13*). The SR pulse was monochromatized to approximately 5eV at  $E_\gamma$  by using a double-crystal Si (333) monochromator and then encountered a sample including  $^{174}\text{Yb}$  nuclei in a cryostat. After passing through the sample, the monochromatized SR pulse encountered a single-crystalline  $\text{YbB}_{12}$  (not enriched  $^{174}\text{Yb}$ ) known as a scatterer. This  $\text{YbB}_{12}$  scatterer was kept at 26K and moved in the triangle mode by a velocity transducer to create a relative Doppler velocity  $\hbar\omega_D$  between the sample and the scatterer. Note that very strong scattering due to electrons in matter occurs promptly after the SR pulse, but the scattering due to resonant nuclear excitation is delayed by the finite lifetime of the excited nuclear state. Thus, we independently observe very weak nuclear resonant scattering in the time-domain measurement. The scattering intensity of the monochromatized SR pulse passing through the sample in the forward direction was measured by these delayed resonant scattering signals from  $^{174}\text{Yb}$  nuclei in the  $\text{YbB}_{12}$  scatterer after each prompt SR pulse using a multi-element Si avalanche

photodiode (APD) detector in the spatially incoherent scattering geometry.

The delayed scattering signal  $S(\hbar\omega_D, \tau)$  after each SR prompt pulse in the nuclear recoil-free absorption process is given by

$$S(\hbar\omega_D, \tau) \propto \int_0^{z^{\text{sc}}} dz \exp(-\mu_e^{\text{sc}} z) \left| \int d\omega \frac{\Gamma_0/2 \exp(-i\hbar\omega\tau/\Gamma_0)}{\hbar(\omega - \omega_D) - i\Gamma_0/2} A^{\text{sa}}(\hbar\omega) A^{\text{sc}}(\hbar\omega, \hbar\omega_D, z) \right|^2, \quad (3)$$

where

$$A^{\text{sa}}(\hbar\omega) = A_0^{\text{sa}} \exp\left(-i \frac{\mu_n^{\text{sa}} z^{\text{sa}} \Gamma_0/2}{\hbar\omega - i\Gamma_0/2}\right),$$

$$A^{\text{sc}}(\hbar\omega, \hbar\omega_D, z) = A_0^{\text{sc}} \exp\left(-i \frac{\mu_n^{\text{sc}} z \Gamma_0/2}{\hbar(\omega - \omega_D) - i\Gamma_0/2}\right),$$

$\tau = t/\tau_0$  is a dimensionless time,  $\tau_0 = \hbar/\Gamma_0$  the lifetime of the excited nuclear state,  $A^{\text{sa}}(\hbar\omega)$  ( $A^{\text{sc}}(\hbar\omega, \hbar\omega_D, z)$ ) represents the radiation amplitude in depth  $z^{\text{sa}}$  ( $z$ ) of the sample (scatterer),  $z^{\text{sa}}$  ( $z^{\text{sc}}$ ) and  $\mu_n^{\text{sa}}$  ( $\mu_n^{\text{sc}}$ ) denote the thickness and the nuclear resonant absorption coefficient of the sample (scatterer), respectively, and  $\mu_e^{\text{sc}}$  represents the electronic absorption coefficient of the scatterer (14). The delayed scattering signals  $S(\hbar\omega_D, \tau)$  were accumulated at each  $\hbar\omega_D$  within the time window from  $\tau_s = t_s/\tau_0$  to  $\tau_e = t_e/\tau_0$  to measure a SR-based Mössbauer absorption spectrum in the energy-domain measurements. Figure A.2(B) shows a delay time spectrum  $S(\tau) (\propto \int S(\hbar\omega_D, \tau) d\omega_D)$  from  $^{174}\text{Yb}$  nuclei in the  $\text{YbB}_{12}$  scatterer measured in our experiment. Since the lifetime of the  $I_e = 2$  excited state of the  $^{174}\text{Yb}$  nucleus is  $\tau_0 = 2.58\text{ns}$ , as seen in Fig. A.2(B), a typical time window in our experiments was in the range from  $\tau_s \sim 3.1$  ( $t_s \sim 8\text{ns}$ ) to  $\tau_e \sim 6.2$  ( $t_e \sim 16\text{ns}$ ) to measure SR-based  $^{174}\text{Yb}$  Mössbauer spectra.

#### A.4 Oscillatory Effects of the Finite-Time Window

The intensity of  $S(\hbar\omega_D, \tau)$  around  $|\hbar\omega_D| \sim 0$  for the  $\text{YbB}_{12}$  sample oscillates as a function of  $\tau$  about the exponential curve as shown in Ref. (15) for  $^{57}\text{Fe}$  Mössbauer resonance where in general,  $|\hbar\omega_D| \sim 0$  means energy near the Mössbauer transition of  $^{174}\text{Yb}$  nuclei in a sample.

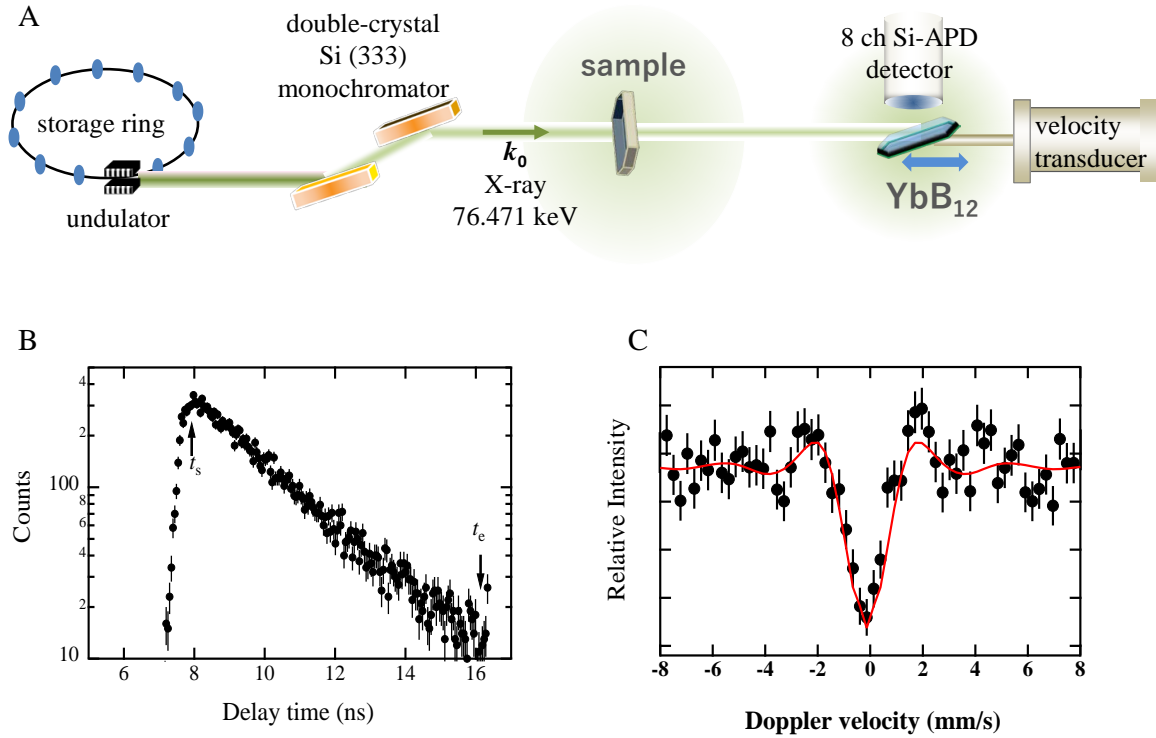


Figure A.2: (A) Schematic illustration of the experimental set up for the synchrotron-radiation-based  $^{174}\text{Yb}$  Mössbauer spectroscopy. The  $^{174}\text{Yb}$  nuclear resonance was obtained by synchrotron radiation using a double-crystal Si (333) monochromator. A sample and the single-crystalline  $\text{YbB}_{12}$  were cooled below 20K and at 26K in each cryostat, respectively. A multi-element Si avalanche photodiode (APD) detector was used to measure delayed incoherent emission from  $^{174}\text{Yb}$  nuclei in the single-crystalline  $\text{YbB}_{12}$  in the spatially incoherent scattering geometry. (B) Typical delay time spectrum of the single-crystalline  $\text{YbB}_{12}$  at 26K. The closed circles with error bar indicate the observed spectrum. (C) Synchrotron-radiation-based  $^{174}\text{Yb}$  Mössbauer spectrum of the powder  $\text{YbB}_{12}$  sample at 20K. The delayed scattering signals were accumulated at each Doppler velocity with the time window from  $t_s$  to  $t_e$  as shown in (B). The closed circles with error bar and the red solid line present the observed and the analytical spectra, respectively.

These oscillations in  $S(\hbar\omega_D, \tau)$  are dynamical effects of scattering processes in the sample and the scatterer. Since the frequencies of the oscillation components vary as  $\hbar\omega_D$ , these oscillation behaviors in  $S(\hbar\omega_D, \tau)$  are smeared out in  $S(\tau)$  as seen in Fig. A.2(B). Experimentally, the intensities at  $\hbar\omega_D$  in a spectrum,  $S(\hbar\omega_D)(= \int_{\tau_s}^{\tau_e} S(\hbar\omega_D, \tau)d\tau)$ , depend not only on  $\hbar\omega_D$  but also on the time window in the accumulation. Thus, a shape of an absorption component in a spectrum is affected by the time window in the accumulation and a Lorentz-function line shape with the expected width should be obtained in a spectrum using a thin-sample with the time window from  $\tau_s \sim 0$  to  $\tau_e \sim \infty$ . Figure A.2(C) shows the SR-based  $^{174}\text{Yb}$  Mössbauer spectrum of the powder  $\text{YbB}_{12}$  (not enriched  $^{174}\text{Yb}$ ) sample at 20K. As seen in this figure, the oscillatory components were observed in background and the full-width at half-maximum of the main absorption component at 0 mm/s was evaluated to be 1.2 mm/s which is much narrower than that ( $2\Gamma_0 = 2.00$  mm/s) expected from  $\tau_0$  of the  $I_e = 2$  excited state of  $^{174}\text{Yb}$  nucleus. These phenomena were observed in the  $^{57}\text{Fe}$  Mössbauer spectra measured by the delayed coincidence method (16) and the SR-based  $^{151}\text{Eu}$  Mössbauer spectroscopy (17), indicating that these are related to the time-window effect in the accumulation of  $S(\hbar\omega_D, \tau)$ . Thus, this time-window effect in the SR-based Mössbauer spectroscopy is important for Mössbauer resonances with short  $\tau_0$ s. The observed SR-based  $^{174}\text{Yb}$  Mössbauer spectrum of  $\text{YbB}_{12}$  is well analyzed using one nuclear transition with this time-window effect and the effective thicknesses of the  $\text{YbB}_{12}$  sample and the scatterer. Since  $\tau_s \sim 3.1$  is much larger compared to  $\tau_s \sim 0$ , then the higher energy resolution than the conventional  $^{174}\text{Yb}$  Mössbauer spectroscopy was achieved in our experiments. The enhanced energy resolution may be essential for extracting time-dependent hyperfine interaction parameters in  $\beta\text{-YbAlB}_4$ .



## B SR-based $^{174}\text{Yb}$ Mössbauer Spectroscopy of Single Crystal $\beta\text{-YbAlB}_4$

### B.1 Experimental Specifics

High-purity single crystals of  $\beta\text{-YbAlB}_4$  were grown by the Al-flux method (18). Energy-dispersive X-ray analysis indicated no impurity phases, no inhomogeneities and a ratio Yb:Al of 1:1 within the detection limits of the equipment. The SR-based  $^{174}\text{Yb}$  Mössbauer experiments were carried out at the BL09XU and BL19LXU beamlines on SPring-8 (see Fig. 1 A of the paper) (13), using SR to excite the  $E_\gamma = 76.471\text{keV}$  Mössbauer transition between the  $I_g = 0$  ground and  $I_e = 2$  excited states of the  $^{174}\text{Yb}$  nuclei contained in the compound. The energy level diagram of the excited  $^{174}\text{Yb}$  nuclear state is sensitive to the surrounding charge configuration and provides real-time information about the Yb valence (see Fig. 1 C of the paper). Measurements were carried out under both ambient and external pressure, and the  $c$ -axis of the single crystalline  $\beta\text{-YbAlB}_4$  samples was aligned along the propagation vector  $\mathbf{k}_0$  of the incident X-ray. Under external pressure, the single crystalline samples were loaded into a sample cavity of the Inconel alloy gasket in a clamp-type diamond-anvil cell (DAC) with ruby crystals and mixtures of methanol-ethanol or Daphne7474 as a pressure-transmitting medium to ensure hydrostatic conditions at 2K. Pressure was calibrated by measuring the wavelength shift of the  $R_1$  luminescence line of the ruby crystals in the clamp-type DAC. Since the sizes of the single crystalline  $\beta\text{-YbAlB}_4$  samples in the sample cavities were comparable with that of the incident X-ray beam, the collimators were used to obtain  $^{174}\text{Yb}$  Mössbauer spectra of satisfactory quality. The high intensity of the incident X-ray made it possible to carry out these experiments without isotopic purification.

Our measurements were performed using cryostat with liquid Helium bath (SM4000 Oxford Instrument). The vibration of the sample/DAC can be ignored within our velocity scale

for  $^{174}\text{Yb}$  Mössbauer spectroscopy. The pressure medium for the diamond-anvil compression was a methanol-ethanol mixture that works best up to about 10 GPa. In liquid media and in spectroscopic and diffraction measurements, this is the preferred medium for diamond-anvil compression. In resistivity measurements, the wire contacts are connected to the sample using conductive paste, which unfortunately reacts with alcohol, so methanol-ethanol mixtures are not used in high-pressure resistivity measurements. Thus there can be sometimes be apparent discrepancies between pressure-dependent transport and spectroscopy measurements that arise due to the different pressure-transmitting media involved.

## B.2 Mössbauer Absorption Line-Shapes

In the  $^{174}\text{Yb}$  Mössbauer effect, the resonance is an electrical quadrupole  $E2$  transition from the  $I_g = 0$  ground to  $I_e = 2$  excited nuclear states. The five nuclear transitions with  $\Delta I^z (= I_g^z - I_e^z) = 0, \pm 1, \text{ and } \pm 2$  are allowed between the ground and excited nuclear states. In no electrical quadrupole and magnetic hyperfine interaction, these five allowed transitions have the same energy and then we observe an absorption component in a Mössbauer spectrum, as seen in Fig. A.2(C). The pure electrical quadrupole interaction splits the  $I_e = 2$  excited nuclear state into three sublevels with  $I_e^z = 0, \pm 1, \text{ and } \pm 2$  within an axial symmetry by

$$\mathcal{H}_Q = \frac{1}{4} \frac{eQV_{zz}}{I_e(2I_e - 1)} [3(I_e^z)^2 - I_e(I_e + 1)], \quad (4)$$

where the second derivative of the potential  $V_{zz} = \partial^2 V / \partial z^2$  is the  $z$  component of the diagonalized electric-field gradient (EFG) tensor and  $Q$  is the nuclear quadrupole moment of the  $I_e = 2$  excited nuclear state of the  $^{174}\text{Yb}$  nucleus. Thus, three allowed nuclear transitions with  $\Delta I^z = 0, \pm 1, \text{ and } \pm 2$  have different energies. In the nuclear resonant scattering using SR, the polarized SR provides the possibility of selective excitations in allowed nuclear transitions. Due to the perfect  $\sigma$ -polarization of the incident X-ray in our experiments, the excitation probabilities in these  $^{174}\text{Yb}$  nuclear transitions are very sensitive to the direction of the  $z$ -axis and

the symmetry of the diagonalized EFG tensor at the Yb site (19).

For  $\beta$ -YbAlB<sub>4</sub> with the orthorhombic  $Cmmm$  structure (18), the principal axes of the diagonalized EFG tensor at one crystallographic Yb site are along the three crystal axes because the local symmetry at the Yb site is  $m2m$ . Since the Yb ions are sandwiched between boron layers and are centered between seven-member boron rings, the principal  $z$ -axis of the diagonalized EFG tensor at the Yb site is parallel to the  $c$ -axis of  $\beta$ -YbAlB<sub>4</sub>, which is the quantization axis  $z_J$  of the hyperfine interactions at the <sup>174</sup>Yb nuclear in  $\beta$ -YbAlB<sub>4</sub>. In our experimental conditions where  $z_J$  at the Yb site in  $\beta$ -YbAlB<sub>4</sub> was parallel to  $\mathbf{k}_0$ , the  $I_g = 0 \rightarrow I_e^z = \pm 1$  nuclear transitions are only selected in the five  $E2$  nuclear transitions of the <sup>174</sup>Yb Mössbauer resonance (19), which have the same energy within an assumption of the axial symmetric EFG tensor.

The possibilities of selective excitations in allowed nuclear transitions and the higher energy resolution are crucial to discuss dynamics of valence fluctuations and the electronic states of the Yb ions in  $\beta$ -YbAlB<sub>4</sub> via the SR-based <sup>174</sup>Yb Mössbauer spectroscopy.

As seen in Figs. 2 A and B of the paper, the broadenings of two nuclear transitions are observed in the SR-based <sup>174</sup>Yb Mössbauer spectra for  $\beta$ -YbAlB<sub>4</sub>, which is attributed to relaxation between two nuclear transitions. In the Mössbauer resonances, a relaxation occurs in the same  $\Delta I^z$  nuclear transitions with different energies caused by time-dependent hyperfine interactions. The Mössbauer absorption line shapes in the presence of the time-dependent hyperfine interactions have been discussed in the stochastic ways (1, 2, 3, 4). In the case of slow relaxation,  $1/\tau_f < 2\varepsilon$ , where  $2\varepsilon$  represents a energy difference between these two nuclear transitions without the relaxation effects and  $\tau_f$  denotes the characteristic timescale in the time-dependent hyperfine interactions, the Mössbauer absorption line shape for two nuclear transitions is expressed in the stochastic model as follow:

$$I(\hbar\omega_D) \propto \left( (1 - R) \frac{\Gamma_0/2 + W + (1/x)(\hbar\omega_D + Wx)}{(\hbar\omega_D + Wx)^2 + (\Gamma_0/2 + W)^2} + (1 + R) \frac{\Gamma_0/2 + W - (1/x)(\hbar\omega_D - Wx)}{(\hbar\omega_D - Wx)^2 + (\Gamma_0/2 + W)^2} \right), \quad (5)$$

where  $2W = 1/\tau_f$ ,  $x = [(\varepsilon/W)^2 - 1]^{1/2}$ , and  $R$  represents small difference in intensity between two nuclear transitions.

In order to combine Eq. 5 with Eq. 3 both amplitude and phase information of  $A^{sa}(\hbar\omega)$  are required. The amplitude  $I(\hbar\omega) \sim |A^{sa}(\hbar\omega)|^2$  is given by Eq. 5. To find the phase, we have fitted Eq. 5 with two Lorentzians which can be easily continued to the complex plane.

Thus the relaxation brings about a broadening and distortions as well as a shift of the absorption lines. For  $1/\tau_f (= 2W) \ll 2\varepsilon$ ,  $I(\hbar\omega_D)$  is the same as two Lorentz-functions centered at  $\hbar\omega_D = \pm Wx \sim \pm\varepsilon$ , which is expected in the absence of any fluctuations in the hyperfine interactions. In the case of fast relaxation,  $1/\tau_f > 2\varepsilon$ , the Mössbauer absorption line shape is given by

$$I(\hbar\omega_D) \propto \left( \frac{(1 + 1/y)(\Gamma_0/2 + W(1 - y))}{(\hbar\omega_D)^2 + (\Gamma_0/2 + W(1 - y))^2} + \frac{(1 - 1/y)(\Gamma_0/2 + W(1 + y))}{(\hbar\omega_D)^2 + (\Gamma_0/2 + W(1 + y))^2} \right), \quad (6)$$

where  $y = [1 - (\varepsilon/W)^2]^{1/2}$ . For  $1/\tau_f (= 2W) \gg 2\varepsilon$ ,  $I(\hbar\omega_D)$  represents a Lorentz-function at  $\hbar\omega_D = 0$  (the first term in eq. (4)). The fluctuations are so fast that the nucleus only feel an average hyperfine interactions. The collapse of a two-peaked structure related to two nuclear transitions occurs in a Mössbauer spectrum as  $2\varepsilon \cdot \tau_f$  is comparable with and then becomes smaller than unity. Accordingly, the two-peaked structure observed in the Mössbauer spectrum manifests slow relaxations in time-dependent hyperfine interactions.

## B.3 Spectral Fits and $^{174}\text{Yb}$ Hyperfine Interactions in $\beta\text{-YbAlB}_4$

### B.3.1 Ambient pressure spectra

The fitting procedures of the SR-based  $^{174}\text{Yb}$  Mössbauer spectra for  $\beta\text{-YbAlB}_4$  were performed using the equations in Section A.3 with two selected nuclear transitions, including the effective thicknesses of the single crystalline  $\beta\text{-YbAlB}_4$  samples and the  $\text{YbB}_{12}$  scatterer and the time-window effect in the time-domain measurements in each experiment (see Section B.1). Figure B.3(A) shows the refined energies  $\varepsilon$  for two  $I_g = 0 \rightarrow I_e^z = \pm 1$  nuclear transitions in

$\beta$ -YbAlB<sub>4</sub> at ambient pressure. As shown in this figure, the energy difference between these nuclear transitions is almost independent of temperature up to 20K.

Mössbauer spectroscopy has been used to discuss electronic states of atoms included Mössbauer isotopes via the nuclear hyperfine interactions. Although there are three main electrical and magnetic hyperfine interactions to determine the energies and the eigenstates of the ground and the excited nuclear states in a Mössbauer isotope, the electrical monopole and electrical quadrupole interactions are important to discuss the electronic state of the atoms in a paramagnetic state. In the experiments using the single crystalline  $\beta$ -YbAlB<sub>4</sub> samples, the degenerate  $I_g = 0 \rightarrow I_e^z = \pm 1$  nuclear transitions are only selected in the five  $E2$  nuclear transitions. In a paramagnetic state with no external magnetic field, the energy of these degenerate nuclear transitions depends on both the electrical monopole and quadrupole interactions. We do not evaluate the electrical monopole and quadrupole interactions for two selected nuclear transitions in  $\beta$ -YbAlB<sub>4</sub> only from the spectrum observed in the experimental condition with  $z_J \parallel k_0$ . Thus, we have measured the SR-based <sup>174</sup>Yb Mössbauer spectrum at 5K in another experimental condition to evaluate the electrical monopole and quadrupole interactions for these two nuclear transitions. In the experiment, the  $c$ -axis of the single crystalline  $\beta$ -YbAlB<sub>4</sub> samples was tilted though 10 deg from the incident X-ray in the horizontal plane, that is, the angle  $\theta$  between  $z_J$  and  $k_0$  was 10 deg.

As shown in Fig. G.8, the characteristic features in the SR-based <sup>174</sup>Yb Mössbauer spectrum observed at 5K with  $\theta = 10$  deg are different from those in the spectrum at 5K with  $\theta = 0$  in Fig. 2 A of the paper, due to the difference of the excitation probabilities in five allowed nuclear transitions between these experimental conditions. The excitation probabilities in these nuclear transitions were evaluated with  $\theta = 10$  deg. We have analyzed the observed SR-based <sup>174</sup>Yb Mössbauer spectrum at 5K using the evaluated excitation probabilities for the five  $E2$  nuclear transitions. In this analysis, furthermore, the  $\tau_f$  value and the energies for the degenerate

$I_g = 0 \rightarrow I_e^z = \pm 1$  nuclear transitions were fixed on those refined from the spectrum observed at 5K with  $\theta = 0$  within the experimental accuracies. The energy  $\varepsilon$  of the  $I_g = 0 \rightarrow I_e^z = \pm 1$  nuclear transition is given by  $\varepsilon = \delta - E_Q/2$  using the isomer shift  $\delta$  and the electrical quadrupole splitting  $E_Q$ . As seen in Fig. G.8, the analytical spectrum agrees well with the observed one. The  $\delta$  and  $E_Q$  values were evaluated to be  $\delta = 0.22$  mm/s and  $E_Q = -2.3$  mm/s and  $\delta = -0.76$  mm/s and  $E_Q \sim 0$  mm/s for two selected nuclear transitions, respectively, by using the stochastic model.

As shown in Fig. B.3(B), the intensity ratio  $R$  between these two selected nuclear transitions is independent of temperature up to 20K within our experimental accuracy. The selected nuclear transitions with  $\delta = 0.27$  mm/s and  $E_Q = -2.3$  mm/s and  $\delta = -0.76$  mm/s and  $E_Q \sim 0$  mm/s correspond to the  $\text{Yb}^{3+}$  and  $\text{Yb}^{2+}$  ionic states, respectively. Since all Yb sites are crystallographically equivalent in  $\beta\text{-YbAlB}_4$ , we assume the same recoil-free fraction (Lamb-Mössbauer factor) of two selected nuclear transitions. The averaged Yb valence was evaluated to be 2.6(1) from the refined  $R$  values, which is in good agreement with those ( $\text{Yb}^{+2.75}$ ) obtained by hard X-ray photoelectron and X-ray absorption near edge structure spectroscopies (8, 20).

Since the nuclear transition for the  $\text{Yb}^{2+}$  state shows a single line feature in the observed spectra, the contribution of the distribution of the ionic and electronic charges in the lattice to  $E_Q$  is negligibly small at the Yb site in  $\beta\text{-YbAlB}_4$  within our experimental energy resolution. The  $E_Q$  value extracted for the  $\text{Yb}^{3+}$  state thus provides information about the crystalline-electric-field (CEF) ground state of the  $\text{Yb}^{3+}$  4f electrons in  $\beta\text{-YbAlB}_4$ . Since the degenerate  $I_g = 0 \rightarrow I_e^z = \pm 1$  nuclear transitions are selected in the experimental condition with  $z_J \parallel \mathbf{k}_0$ , the assumption of the axial symmetric EFG is reasonable within our experimental energy resolution. The  $E_Q^{4f}$  due to the interaction between the nuclear quadrupole moment  $Q$  and the quadrupole moment of the CEF ground state of rare-earth 4f electrons is given by

$$E_Q^{4f} = -\frac{1}{4}e^2Q(1 - R_Q)\langle J || \alpha || J \rangle \langle r^{-3} \rangle_{4f} \langle 3J_z^2 - J(J+1) \rangle, \quad (7)$$

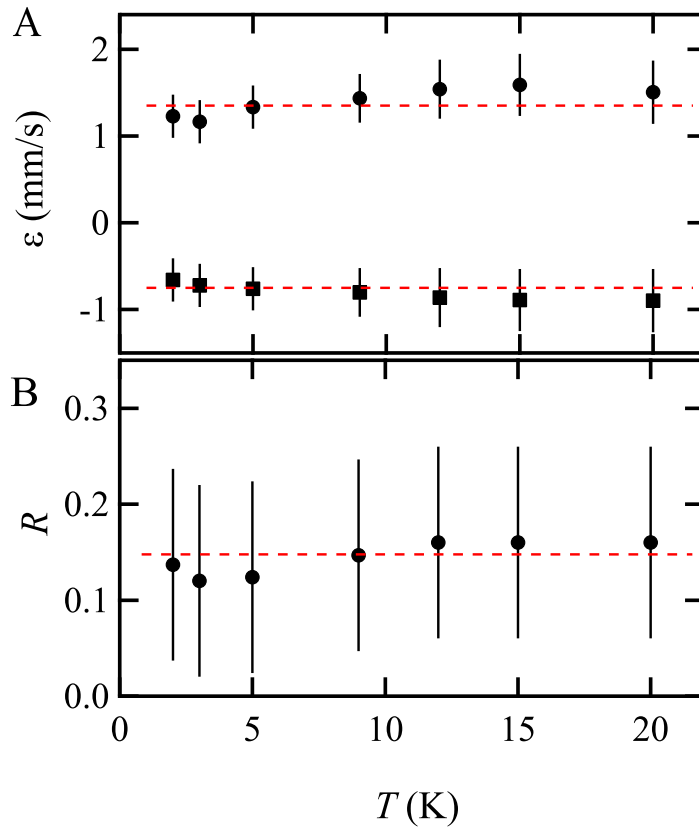


Figure B.3: (A) Refined energies  $\varepsilon$  for two selected  $I_g = 0 \rightarrow I_e^z = \pm 1$  nuclear transitions and (B) difference in intensity  $R$  between these two nuclear transitions in  $\beta$ -YbAlB<sub>4</sub> as functions of temperature. The red broken lines are visual guides.

where  $\langle r^{-3} \rangle_{4f}$  is the averaged value of  $r^{-3}$  for the  $4f$  electrons in a given  $J$  state for a rare-earth ion,  $\langle J || \alpha || J \rangle$  represents a reduced matrix element defined by the operator equivalent and  $R_Q$  is the shielding factor (21). The states of the  $\text{Yb}^{3+}$   $4f$  electrons are split to four Kramers doublets by the CEF interaction. In the case where  $J_z$  is conserved, the expected  $E_Q^{4f}$  values are evaluated to be  $-14.7$ ,  $-2.1$ ,  $6.3$ , and  $10.5$  mm/s for the four Kramers doublets with  $J_z = \pm 7/2$ ,  $\pm 5/2$ ,  $\pm 3/2$ , and  $\pm 1/2$ , respectively, using  $\langle r^{-3} \rangle_{4f} = 13.83$  a.u., and  $R_Q = 0.21(1)$  with  $\langle J || \alpha || J \rangle = 2/63$  for  ${}^2F_{7/2}$  and  $Q = 2.12$  b (22, 23). As the result of the extracted  $E_Q$  value for the  $\text{Yb}^{3+}$  state, the ground Kramers doublet for the  $\text{Yb}^{3+}$   $4f$  electrons is almost pure  $J_z = \pm 5/2$  states in  $\beta\text{-YbAlB}_4$  with a negligible admixture of the  $J_z = \pm 1/2$  state.

### B.3.2 Finite pressure, low temperature spectra.

As seen in Fig. 2 B of the paper, the similar two-peaked structure was observed in the SR-based  ${}^{174}\text{Yb}$  Mössbauer spectra at 0.25 and 0.7 GPa at 2K. It was confirmed by the SR X-ray diffraction measurements of  $\beta\text{-YbAlB}_4$  under pressure (24) that the structural symmetry and the individual atomic coordination parameters do not change up to 3.5 GPa at 7K. Thus, the characteristic change in the features of the observed spectra around  $\sim 1$  GPa is not related to a pressure-induced structural transition in  $\beta\text{-YbAlB}_4$  at 2K. The observed spectra below 1.2 GPa at 2K were analyzed by using the same stochastic model like that at ambient pressure (see Section A.3 and B.2). As seen in Figs. 2 A and B of the paper and Fig. A.2(C), the absorption component observed in the SR-based  ${}^{174}\text{Yb}$  Mössbauer spectrum at 2.3 GPa and 2K is much narrower than that in the spectrum at 20 K and ambient pressure and comparable with that in the spectrum of  $\text{YbB}_{12}$ . The observed spectrum at 2.3 GPa and 2K was analyzed using a single absorption component (see Section B.2). Figure G.9(A) shows the refined energies  $\varepsilon$  for two  $I_g = 0 \rightarrow I_e^z = \pm 1$  nuclear transitions up to 1.2 GPa at 2K and the refined absorption-peak position at 2.3 GPa and 2K in  $\beta\text{-YbAlB}_4$ . As shown in Fig. G.9(B), the intensity ratio  $R$



between these two selected nuclear transitions is independent of pressure up to 1.2GPa at 2K within our experimental accuracy. The absorption-peak position at 2.3GPa and 2K corresponds to the weighted average of two absorption-peak positions below 1.2GPa at 2K, revealing that the averaged electronic state of the Yb ions in  $\beta$ -YbAlB<sub>4</sub> is not changed by pressure up to  $\sim$ 2.3GPa at 2K.

Since the <sup>174</sup>Yb Mössbauer spectrum at 2.3GPa and 2K was well reconstructed by a Lorentz-function,  $1/\tau_f \gg 2\varepsilon$  in the stochastic relaxation model. The width of the absorption component of  $\beta$ -YbAlB<sub>4</sub> sample was refined to be  $\Gamma = 1.11(1)$ mm/s at 2.3GPa and 2K, which is broader than  $\Gamma_0 = 1.00$ mm/s expected from  $\tau_0$  of the  $I_e = 2$  excited state of the <sup>174</sup>Yb nucleus. If we assume that this broadening comes from the relaxation between two nuclear transitions,  $\Gamma$  is given by

$$\Gamma = \Gamma_0 + 2W(1 - y) \sim \Gamma_0 + \frac{\varepsilon^2}{2}\tau_f$$

from the first term of eq. (4). The energy difference  $2\varepsilon$  between two  $I_g = 0 \rightarrow I_e^z = \pm 1$  nuclear transitions was estimated to be  $2\varepsilon \sim 2.2(6)$  mm/s from the refined energies  $\varepsilon$  for two  $I_g = 0 \rightarrow I_e^z = \pm 1$  nuclear transitions for the Yb<sup>3+</sup> and Yb<sup>2+</sup> ionic states at ambient pressure and below 1.2GPa at 2K. We have evaluated  $\tau_f \sim 0.04\tau_0$  ( $\sim 0.1$ ns) at 2.3GPa and 2K. In Mössbauer absorption experiments, the broadening from  $\Gamma_0$  in the width of the Lorentz-function could occur due to the effective thickness of a Mössbauer isotope in a sample. Thus, the evaluated  $\tau_f$  value is maximum one for  $\beta$ -YbAlB<sub>4</sub> at 2.3GPa and 2K.

## B.4 Statistical Analysis of the Spectra

The entire focus of our paper involves the resonant Mössbauer absorption spectra that lie at low Doppler velocity below  $\pm 2$ mm/s. In this region, the X-ray scattering off the nuclei is unitary and the only source of error is the photon count. By contrast, the off-resonance Mössbauer signals at large Doppler shift are dominated by multiple elastic scattering, leading to interference

effects that give rise to systematic errors in the data that are absent at low Doppler shift. This leads to modulations in background signal as a function of Doppler velocity that are related to the finite sample ( $\beta$ -YbAlB<sub>4</sub>) and absorber (YbB<sub>12</sub>) thicknesses, and the finite time window for photon counts (25, 17, 12, 14).

Now we turn to the analysis of the resonant Mössbauer absorption. There are two aspects of the data that we wish to highlight that clearly demonstrate a signal that rises well above the noise level. There are two i

#### B.4.1 Broadening of the Lineshape at low temperature

A plot of FWHM of the spectral dip as a function of temperature and pressure (Fig. G.10) clearly shows that the width of absorption line broadens at low temperatures and pressures. This is in marked contrast with the fact that the spectral peaks usually broaden at high temperatures. Furthermore, the evolution of the FWHM vs. pressure correlates with transition between a strange metal to a Fermi liquid in previous transport experiments.

#### B.4.2 Statistical significance of double-peak structure

We have done a thorough statistical analysis of the data. The quality of the fit is dependent on the regression and total sum of squares, given by

$$SSR = \frac{1}{N} \sum_{i=1}^N (y_i - f_i)^2, \quad SST = \frac{1}{N} \sum_{i=1}^N (y_i - \bar{y})^2 \quad (8)$$

where  $y_i$  is the data,  $f_i$  is the fit to data,  $\bar{y} = \frac{1}{N} \sum_i y_i$  is the average of the data set and  $N$  is the number of data points. These variables are used to compute the standard error via  $\sigma_{tot} = \sqrt{SSR}$ . However, it is more systematic to define two new parameters  $R^2$  and adjusted  $\bar{R}^2$  parameters:

$$R^2 = 1 - \frac{SSR}{SST}, \quad \bar{R}^2 = 1 - \frac{N-1}{N-P-1} (1 - R^2) \quad (9)$$

where the latter compensates for the number of fitting parameters,  $P$ .

Fig. G.11(A) shows the attempt to fit the experimental lineshape using a single Gaussian or Lorentzian peak. Such single-peak fits do not capture the data in either the central region or the tails, as quantified by the low values of  $R^2$  and  $\bar{R}^2$ . If, following Referee 3. we disregard the key central region as noise, we can fit the tails using a Gaussian or Lorentzian lineshape, providing a noise background against which we can assess the probability that the splitting is a statistical anomaly. This fit is shown in blue in Fig. G.11(B).

The blue baseline, based on the assertion that there is no splitting allows us to now assess whether the observed deviation from a single peak is statistically significant. The error bars in the measurement have been reliably established from the standard deviation in photon counts. Taking the pessimistic assumption that each deviating point is the result of Gaussian noise about the single peak background, we then have two points with a standard deviation of  $2\sigma$  a central point with a standard deviation of  $3\sigma$ . The probability of this deviation is then given by

$$\mathcal{P} = \mathcal{E}(2\sigma)^2 \mathcal{E}(3\sigma) \equiv \mathcal{E}(4.84\sigma) \quad (10)$$

where

$$\mathcal{E}(x) = \frac{1}{\sqrt{2\pi}\sigma} \int_x^\infty e^{-\frac{x^2}{2\sigma^2}}. \quad (11)$$

In other words, this data represents a  $4.84\sigma$  event, an event that would occur less than one in a million experiments. This analysis, combined with the other data that shows a systematic broadening at low temperatures and low pressures establishes that our results meet the gold standard ( $5\sigma$ ) for statistically significant experimental observations.

By contrast, the double-peak fit to the data, a fit grounded in the Anderson-Kubo formula for dynamical fluctuation, is significantly more successful, as shown in Fig. G.11(C). It is these fits that were used to extract the valence fluctuation rate  $\tau_f^{-1}$ . Comparing the  $R^2$  and  $\bar{R}^2$  of these fits, we conclude that first the analytical Kubo-Anderson fit and next a Gaussian fit are the best

fits to the data.

## B.5 Lamb-Mössbauer factor on $^{174}\text{Yb}$ nuclei in $\beta\text{-YbAlB}_4$

The Lamb-Mössbauer factor  $f_{\text{LM}}$  describing the recoil-free fraction of the nuclear absorption, is related to atomic motions for Mössbauer isotopes in a matter. The  $f_{\text{LM}}$  is generally described by

$$f_{\text{LM}} = \langle \exp[i(\mathbf{k}_0 - \mathbf{k}_f) \cdot \mathbf{r}] \rangle = \exp[-\langle [\mathbf{k}_0 \cdot \mathbf{r}]^2 \rangle] = \exp[-k_0^2 \langle \Delta z^2 \rangle], \quad (12)$$

where  $\Delta z$  is an atomic displacement from a regular position in a matter along the direction of  $\mathbf{k}_0$ . In scattering experiments, this is the effects of the zero point and temperature motions of the atom bound in a matter. The temperature dependence of  $f_{\text{LM}}$  is

$$f_{\text{LM}}(T) = \exp \left( -E_{\text{R}} \int_0^\infty \frac{F(E)}{E} \coth \frac{\beta E}{2} dE \right) \quad (13)$$

using the local (partial) phonon density of states  $F(E)$  for a Mössbauer atom, where  $\beta = \frac{1}{k_{\text{B}}T}$ ,  $k_{\text{B}}$  is Boltzmann constant and  $E_{\text{R}} (= \frac{E_{\gamma}^2}{2mc^2})$  recoil energy. In the Debye approximation for  $\nu(E)$ ,  $f_{\text{LM}}(T)$  becomes

$$f_{\text{LM}}(T) = \exp \left( -\frac{6E_{\text{R}}}{k_{\text{B}}\Theta_{\text{D}}} \left[ \frac{1}{4} + \left( \frac{T}{\Theta_{\text{D}}} \right)^2 \int_0^{\Theta_{\text{D}}/T} \frac{x}{e^x - 1} dx \right] \right). \quad (14)$$

In the case of  $T \ll \Theta_{\text{D}}$ ,  $f_{\text{LM}}(T)$  has a formula of

$$f_{\text{LM}}(T) = \exp \left( -\frac{E_{\text{R}}}{k_{\text{B}}\Theta_{\text{D}}} \left[ \frac{3}{2} + \left( \frac{\pi}{\Theta_{\text{D}}} \right)^2 T^2 \right] \right). \quad (15)$$

In SR-based Mössbauer spectroscopy, the relative intensity  $I$  integrated in the energy region of the spectrum with absorption components for a sample is proportional to the number and  $f_{\text{LM}}$  of Mössbauer resonant nuclei in the sample. The same single crystalline  $\beta\text{-YbAlB}_4$  sample was used in our SR-based  $^{174}\text{Yb}$  Mössbauer experiments at ambient pressure. The size of this sample was much larger than that of the incident X-ray beam, indicating that the number of  $^{174}\text{Yb}$  nuclei

in the beam was same in our experiments. We have evaluated  $I$  proportional to  $f_{\text{LM}}(T)$  from the observed SR-based  $^{174}\text{Yb}$  Mössbauer spectra at ambient pressure with correction of scattering conditions including the time-window effects.

In our experiments under pressure at 2K, as seen in Fig. 2 B of the paper,  $^{174}\text{Yb}$  Mössbauer spectra of satisfactory quality were obtained by using the collimators to absorb incident X-ray photons without passing through the single crystalline  $\beta\text{-YbAlB}_4$  sample in the clamp-type DAC, which were made by Re and Pb metals with 250 and 800 $\mu\text{m}$  thickness, respectively. Although the thicknesses of these samples were same within our experimental accuracies, the transmission intensities of the incident X-ray photons with  $E_\gamma$  were slightly different though these collimators. We have corrected these absorption effects to evaluate  $I$  proportional to  $f_{\text{LM}}(p)$  from the observed SR-based  $^{174}\text{Yb}$  Mössbauer spectra.

## C Reproducibility after Thermal Cycling

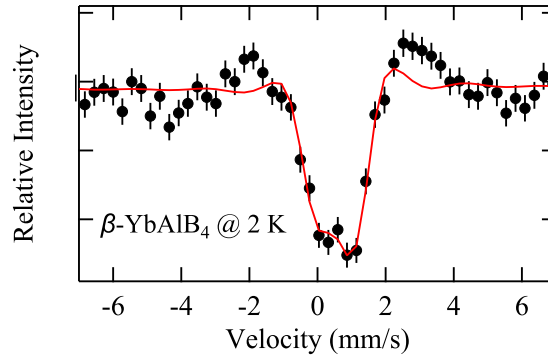


Figure C.4: Mössbauer spectra of the same  $\beta\text{-YbAlB}_4$  sample studied in the paper after a thermal cycling at 2K under ambient pressure to confirm the reproducibility of the splitting. For comparison, the analytical curve in red is the same fit as that used in the 2K ambient pressure data in the paper (Fig 2A in paper).

Fig. C.4 shows the result of Mössbauer spectroscopy of the the same  $\beta\text{-YbAlB}_4$  sample studied in the paper in a different thermal cycle at 2K and under ambient pressure. Although

the details have changed the characteristic double-peak feature persists.

## D Recent Characterization of Samples using Bulk Probes

In this section, we briefly present new thermodynamical data taken from recently grown  $\beta$ -YbAlB<sub>4</sub> crystals, similar to the ones used for the Mössbauer spectroscopy. As seen in Fig. D.5, the absence of any thermodynamic transition in  $M/H$  and  $C/T$  support the interpretation of the Mössbauer data as discussed in the next section. Fig. D.6 indicates the sharpness of superconducting transition for the same samples.

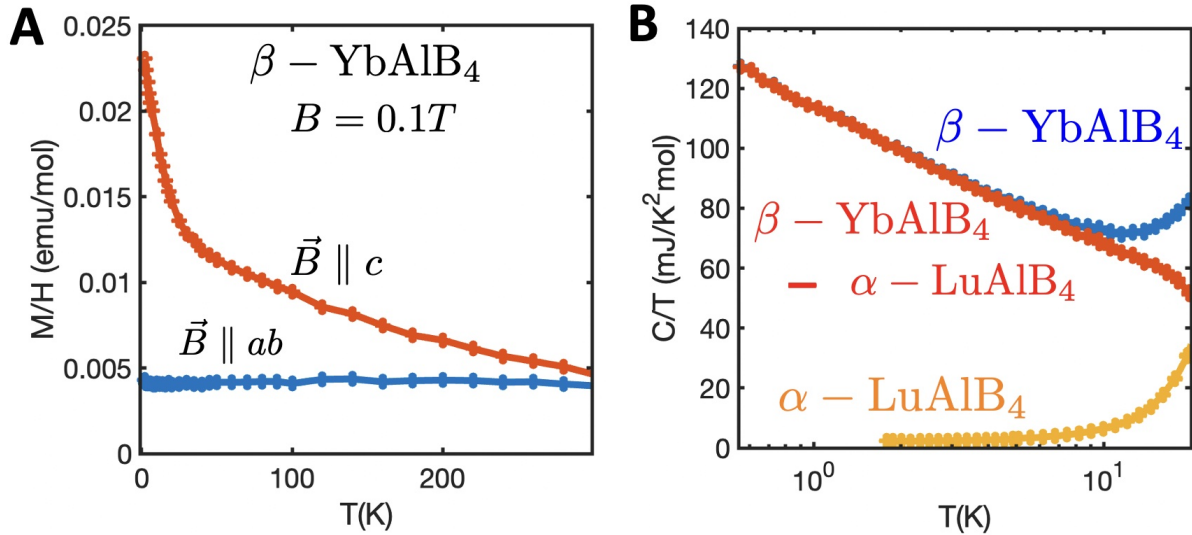


Figure D.5: (A) Magnetic susceptibility vs. temperature for field parallel to ab-plane and c-axis. (B) Heat capacity of  $\beta$ -YbAlB<sub>4</sub> and  $\alpha$ -LuAlB<sub>4</sub>. The latter is subtracted from the former to get the electronic contribution to the  $C/T$  shown in red.

## E Excluded Possibilities for Observed Results

In the following we discuss a series of cross-checks to confirm the overall consistency of the results and that support of the charge fluctuation interpretation of the data.

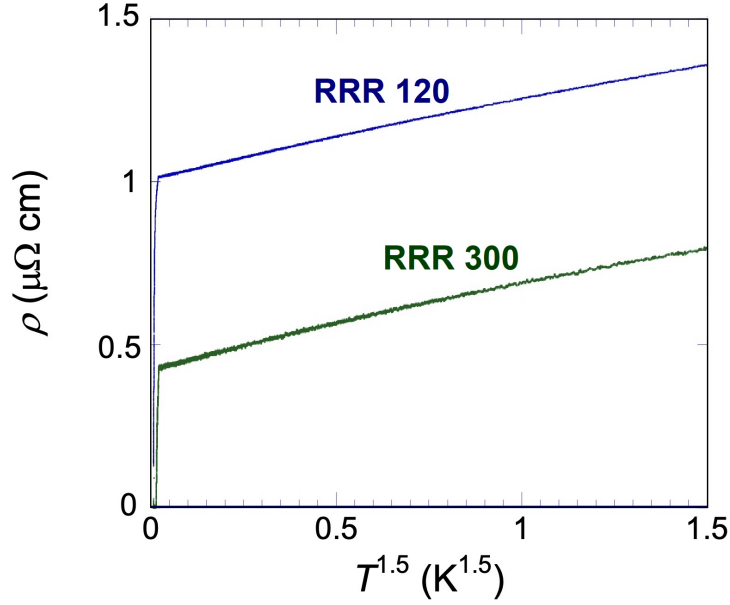


Figure D.6: Resistivity of  $\beta$ -YbAlB<sub>4</sub> as a function of temperature for two different residual resistivity ratios (RRRs). Note the sharpness of the superconducting transition for the selected single crystals with RRR > 100 used in our Mössbauer experiments.

- **Nuclear Origins.** The quantization axis  $z_J$  of the diagonalized electric-field gradient (EFG) tensor at the Yb site with the  $m2m$  local symmetry is parallel to the  $c$ -axis of  $\beta$ -YbAlB<sub>4</sub> with an orthorhombic  $Cmmm$  structure, indicating  $z_J \parallel \mathbf{k}_0$  in our experiments. As a result of the angular momentum selection rule, only a single degenerate nuclear transition  $I_g = 0 \rightarrow I_e^z = \pm 1$  is probed out of the five  $E2$  nuclear transitions ( $\Delta I^z = 0, \pm 1$ , and  $\pm 2$ ) of the <sup>174</sup>Yb Mössbauer resonance (see Section B.2) (19).
- **Magnetic Origins** The absence of long-range magnetic order in  $\beta$ -YbAlB<sub>4</sub> (26, 27) rules out magnetic hyperfine interactions as the origin of this splitting. Generally, the electrical monopole interaction in the hyperfine interaction is related to a valence state of a rare-earth ion.

- **Disorder.** All Yb sites are crystallographically equivalent in  $\beta$ -YbAlB<sub>4</sub> and it is known, from the SR X-ray diffraction measurements (24), that the structural  $Cmmm$  symmetry and the individual atomic coordination parameters do not change up to 3.5GPa at 7K. Moreover, the residual resistivity ratio RRR more than 100 reveals that there is no quenched disorder in this material at low temperature.
- **Antiferroquadrupolar (AFQ) Order.** From the Mössbauer spectra alone, it is not possible to exclude the scenario of an AFQ configuration with staggered electric field gradients. However such a state of long-range order can be directly ruled out from other observations. Such quadrupolar transitions are well known in other heavy fermion systems (e.g. UPd<sub>3</sub> (28) and CeB<sub>6</sub> (29)) where they lead to a singularity in the specific heat and a cusp in the resistivity. Neither features are observed. Finally, there is no signature of any quadrupolar structural change in the high resolution X-ray diffraction patterns.
- **Charge Density Wave Scenario** There are two good reasons why a charge density wave (CDW) scenario can be ruled out as an explanation for the observed effects we present here:

First, there is no evidence in  $\beta$ -YbAlB<sub>4</sub> for any phase transition into a partially gapped phase in either transport or thermodynamic measurements (Figs. D.5,D.6), which all display smooth evolution as a function of decreasing temperature with no observable discontinuities or other features.

More generally, we can rule out any ordered frozen configurations, which would have produced a thermodynamic signal. The alternative, disordered frozen configurations would play the role of quenched disorder, a possibility that is ruled out by the tiny residual resistivity of less than  $1\mu\Omega\text{cm}$  in the  $\beta$ -YbAlB<sub>4</sub> samples used in the Mössbauer experiments.



Second, the observed isomer shift in the Mössbauer spectra is inconsistent with a CDW. Isomer shifts result from small modifications of nuclear excitation spectra induced by changes in the occupancies of orbitals with significant atomic penetration. 3d orbitals of transition metals and 4f-orbitals of rare earth atoms that penetrate deep into an atom, “communicating” their valence to the nucleus via their Coulomb-coupling to the innermost s-orbitals. The observed isomer shifts for  $^{174}\text{Yb}$  Mössbauer isotopes,  $\text{Yb}^{2+}$  and  $\text{Yb}^{3+}$  ions are separated by about 1mm/s [see W. Henning, *et al.* *Z. Phys.* **241** 138 (1971)], and the splitting observed to develop between the two peaks in the spectrum of  $\beta\text{-YbAlB}_4$  at 2 K is of the same order. A CDW would typically occur in a conduction band orbital that does not penetrate far inside the atom and thus does not influence the nuclear spectrum; moreover, a CDW typically involves a fractional modulation in charge, far smaller than the integral charge required to produce known isomer shifts.

- **Relaxational Broadened Static Double Peak** Finally, one may envision a relaxational broadening mechanism to account for the discrepancy of the static fit to the lineshape. An electronic relaxation broadening mechanism, produced for example by a phonon-induced change in the Yb environment would have to be slow on a Mössbauer time scale to broaden the peaks. Mössbauer spectroscopy averages the environment of the nucleus over time-scales of order a nano-second. Anything faster than this scale simply leads to a single, motionally narrowed absorption line. To avoid this fate, a relaxational excitation would have to operate at the micro-volt scale, a scale that is orders of magnitude smaller than the characteristic scale of collective electronic or lattice excitations.
- **Mixture of Nuclear Transitions.** By varying the incident angle of the X-ray w.r.t. to the c-axis to 10 deg, it is possible to excite other nuclear transitions which have different energies due to different coupling to the electronic degrees of freedom and to allow us to

extract the the isomer (electrical monopole) shift  $\delta$  and the electrical quadrupole splitting  $E_Q$  shifts (see Section B.2 and B.3). For the two different charge states of Yb ions in  $\beta$ -YbAlB<sub>4</sub>, these values were estimated to be  $\delta = 0.27$  mm/s and  $E_Q = -2.3$  mm/s and  $\delta = -0.72$  mm/s and  $E_Q = 0$  mm/s for two selected <sup>174</sup>Yb nuclear transitions, respectively. Since the total angular momentum  $J$  is a good quantum number, the electrical quadrupole interaction derives from the nonspherical  $4f$  electron distribution (30). The second of these transitions with  $E_Q = 0$  corresponds to the nuclear transitions of the isotropic ( $J = 0$ ) Yb<sup>2+</sup> ion with <sup>1</sup>S<sub>0</sub>. The difference in  $\delta$  between these nuclear transitions is comparable with that between the Yb<sup>3+</sup> and Yb<sup>2+</sup> ionic state reported by the conventional <sup>174</sup>Yb Mössbauer spectroscopy (31). Furthermore, these extracted  $\delta$  values are compatible with the electron densities at the Yb nuclei for the Yb<sup>2+</sup> and Yb<sup>3+</sup> ionic states in  $\beta$ -YbAlB<sub>4</sub> calculated by using the full-potential Korringa-Kohn-Rostoker method (32, 33). Thus, the selected nuclear transition with  $\delta = 0.27$  mm/s and  $E_Q = -2.3$  mm/s is identified as the nuclear transition of the Yb<sup>3+</sup> configuration with <sup>2</sup>F<sub>7/2</sub>.

Recent experimental results and theoretical predictions find a strongly anisotropic hybridization between the Yb  $4f$  electrons and conduction electrons in  $\beta$ -YbAlB<sub>4</sub>, suggesting its pure  $J_z = \pm 5/2$  ground doublet states (26, 34, 35), attributed to the crystalline-electric-field (CEF) ground state of the Yb  $4f$  electrons. Interestingly, the extracted  $E_Q$  value indicates that the ground Kramers doublet is almost pure  $J_z = \pm 5/2$  states (see Section IV-a). The CEF ground state of the Yb<sup>3+</sup>  $4f$  electrons inferred from our Mössbauer studies is thus fully consistent with both the theoretical material modeling, the single-ion crystal field analysis (34, 36) and recent Core-level spectroscopy measurements (37).

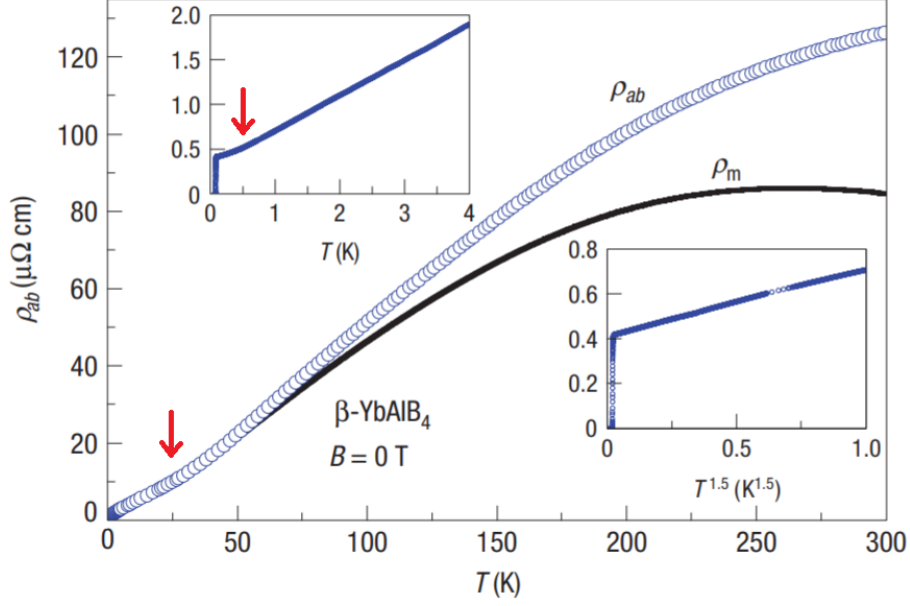


Figure F.7: The resistivity of  $\beta$ -YbAlB<sub>4</sub> showing  $\rho \sim T$  for over the range 0.5-25K (as labeled by arrows) and a slightly different slope over the range 25K to 150K, from (38).

## F Planckian Dissipation in $\beta$ -YbAlB<sub>4</sub>

We now establish that the strange metal regime of  $\beta$ -YbAlB<sub>4</sub> lies in the Planckian dissipation regime. The resistivity in the temperature range between 0.25K and 25K reported in (38), [Fig.] has a linear temperature dependence. From these data, we extract

$$\rho = \rho_0 + A_\rho T, \quad \text{where} \quad A_\rho = 0.4 \mu\Omega\text{cm}/K \quad 0.5K < T < 25K. \quad (16)$$

We use the Drude formula

$$\sigma = \frac{ne^2\tau_{tr}}{m} \quad \rightarrow \quad \frac{1}{\tau_{tr}} = \frac{ne^2\rho}{m} \quad (17)$$

to find the scattering rate. The effective mass can be eliminated using Fermi temperature:

$$\left(\frac{1}{\tau_{tr}}\right)_{3D} = \frac{k_B T}{\hbar} \times \zeta, \quad \zeta = \frac{A_\rho^2 T_F}{h/2e^2}, \quad (18)$$

In  $\beta$ -YbAlB<sub>4</sub>, the lattice parameters are  $a = 0.73\text{nm}$ ,  $b = 0.93\text{nm}$  and  $c = 0.35\text{nm}$ . Therefore, the system is relatively three-dimensional. Nevertheless, we have cast the scattering rate in

terms of an effective “sheet density”  $A_\rho^\square \equiv A_\rho(3\pi^2n)^{1/3}$  so that the results can be compared to those of Cuprate (39). We assume that each unit cell contributes roughly one electron to the charge density, i.e.  $n \sim 6 \times 10^{27}m^{-3}$ . This is consistent with our measurements the Hall effect (40). The Fermi temperature is obtained directly from the heat capacity  $C = \gamma T$  with  $\gamma = \pi^2 k_B^2 \nu(\epsilon_F)/3$  which can be written as

$$\gamma_{3D} = \frac{\pi^2}{2} k_B \frac{nV}{T_F} \quad (19)$$

Considering  $\gamma = 0.1 \text{ J/K}^2/\text{mole}$  (38), we have to set  $k_B nV = k_B N_A = 8.3$ , finding  $T_F = 273\text{K}$  in the 3D model, small but plausible values for a heavy-fermion metal. Finally,

$$\left(\frac{1}{\tau_{tr}}\right)_{3D} = \frac{k_B T}{\hbar} \times \zeta, \quad \zeta = 0.4 \quad (20)$$

While the precise value of  $\zeta$  depends on the assumptions of the model, the important point is that it is a constant of  $\zeta \sim O(1)$ . Above 25K the increased linear resistivity coefficient corresponds to  $\tau_{tr}^{-1} = 0.63\tau_{Pl}^{-1}$  ( $25\text{K} < T < 150\text{K}$ ) in terms of the Planckian scattering rate  $\tau_{Pl}^{-1} = k_B T/\hbar$ . As discussed in the paper, the change in the slope of linear resistivity is correlated with the change in the dynamics of phonons. The appearance of a transport scattering rate of order  $k_B T/\hbar$  is the hallmark of a Planckian metal.

## G Supporting Theoretical Discussion

### G.1 Kondo Breakdown

The Kondo breakdown scenario can be captured by a number of approaches, including the slave-boson hybridization (41), the numerical renormalization group studies of the pseudogap single-impurity Anderson model (42) or Schwinger boson large-N study of the Kondo lattice (43). Fig. G.12(A) shows the divergence of the charge susceptibility at a Kondo breakdown transition

studied with the latter method. Within a simple Anderson model

$$H_{\text{Anderson}} = H_c + U_0(n_d)^2 + \sum_{\sigma=\uparrow,\downarrow} V_0(c_{k\sigma}^\dagger d_\sigma + h.c.) + \mu_d n_d, \quad n_d = \sum_{\sigma=\uparrow,\downarrow} d_\sigma^\dagger d_\sigma, \quad (21)$$

the hybridization and the interaction are renormalized  $V_0 \rightarrow V = ZV_0$  and  $U_0 \rightarrow 0$  due to the Kondo effect, where the wavefunction renormalization  $Z$  is given by

$$Z = [1 - \partial_\omega \Sigma_f(\omega)]^{-1}. \quad (22)$$

At the Kondo-breakdown transition, the localization of the  $d$  electrons means that their effective mass diverges and the  $Z \rightarrow 0$ , further renormalizing the hybridization to zero  $V \rightarrow 0$  (41, 42, 43). The fluctuation time-scale is associated with the hybridization  $V = ZV_0$

$$\tau_f^{-1} \sim \pi \rho V^2 \quad (23)$$

where  $\rho$  is the density of states of the conduction electrons at the Fermi energy. Therefore, the renormalization  $V \rightarrow 0$  at the Kondo break-down leads to slow charge fluctuations.

Fig. G.12(A) shows the static charge susceptibility vs. temperature across a Kondo break-down transition between a FL phase and a spin-liquid, computed using Schwinger boson approach (43). The  $\chi_\rho \sim 1/T$  at the transition indicates to the emergence of a sharp zero-frequency peak in the dynamical charge susceptibility  $-\beta\chi_\rho''(\omega)/\omega$ , as shown in the inset of Fig. G.12(B). Fig. G.12(B) also shows the result of this critical charge susceptibility on the Mössbauer line shape where a single peak at high temperature is splitted into two peaks proportional to  $\alpha^2$ .

In spite of qualitative agreement, the splitting observed in the paper is too large compared to the temperature and cannot be entirely accounted for by the mechanism discussed here.

The resolution of this paradox involves the role of electron-phonon coupling: The phonons respond to the charge accumulation by dressing the charges into polarons, thereby additionally renormalizing the hybridization and thus the width of the dynamical charge susceptibility.

## G.2 Phonons and Polarons

The physical essence can be captured by a very simplified model

$$H = H_{\text{Anderson}} + \sum_q [\omega_q a_q^\dagger a_q + g_q (a_q^\dagger + a_q) n_d]. \quad (24)$$

The normal phononic modes are related to the crystal displacement and momentum as

$$\Delta z = \sum_q \sqrt{\frac{\hbar}{2m\omega_q}} (a_q + a_q^\dagger), \quad p_z = \sum_q i \sqrt{\frac{\hbar m \omega_q}{2}} (a_q^\dagger - a_q) \quad (25)$$

The phonon mode is approximated by the Debye model with a characteristic energy scale  $k_B \Theta_D$  and  $g_q$  is the coupling of the phonons  $\omega_q$  to the occupation of the  $f$ -electrons. The effect of polarons is non-perturbative in  $g_q$  and can be best captured by the so-called Lang-Firsov unitary transformation (44)

$$U = \exp\left[\sum_q u_q (a_q^\dagger - a_q) n_d\right], \quad (26)$$

where  $n_d = \sum_\sigma d_\sigma^\dagger d_\sigma$ . As a result of this transformation, we have

$$V \rightarrow V e^{\sum_q u_q (a_q^\dagger - a_q)}, \quad g_q \rightarrow g_q - u_q \omega_q, \quad U \rightarrow U - \sum_q \omega_q u_q^2. \quad (27)$$

Therefore, choosing  $u = g_q/\omega_q$  eliminates the electron-phonon coupling. But the hybridization is renormalized:

$$V \rightarrow V \langle e^{\sum_q u_q (a_q^\dagger - a_q)} \rangle = V e^{-\sum_q u_q^2 (n_q + 1/2)}. \quad (28)$$

Here,  $n_q$  is the number of bosons  $\omega_q$  and it is given by the Bose-Einstein distribution in a thermal state  $n_q = n_B(\omega_q)$  where  $n_B(\omega) = [1 + e^{\omega/T}]^{-1}$  at temperature  $T$ . At low-temperature thermal fluctuations are suppressed  $n_B(\omega_p) = 0$ , and only the quantum fluctuations contribute to the suppression of the renormalized matrix element of the hybridization  $V$ . Note that as a result of the unitary transformation

$$a_q^\dagger a_q \rightarrow U^\dagger a_q^\dagger a_q U = (a_q^\dagger - u_q n_d)(a_q - u_q n_d) = a_q^\dagger a_q - u_q n_d (a_q^\dagger + a_q) + u_q^2 n_d^2. \quad (29)$$

Therefore, the phonon occupancy departs from the thermal equilibrium to  $n_q = \langle a_q^\dagger a_q \rangle = n_B(\omega_q) + u_q^2 n_d^2$ . For simplicity, we limit the discussion to the transition between empty ( $n_d = 0$ ) and singly occupied ( $n_d = 1$ ) infinite-U Anderson model. Therefore, the quantum fluctuation contribution  $N_p \equiv \sum_q u_q^2$  in the exponent of Eq. (28) can be interpreted as the total number of phonons excited by the change in the charge  $n_d = 0 \rightarrow n_d = 1$  and involved in the polaron. This leads to the additional slowing-down of the charge fluctuations

$$\tau_f^{-1} \sim \pi \rho V^2 e^{-2N_p}. \quad (30)$$

This discussion and the interpretation of  $N_p$  as the number of phonons excited by the charge goes back to (45, 46).

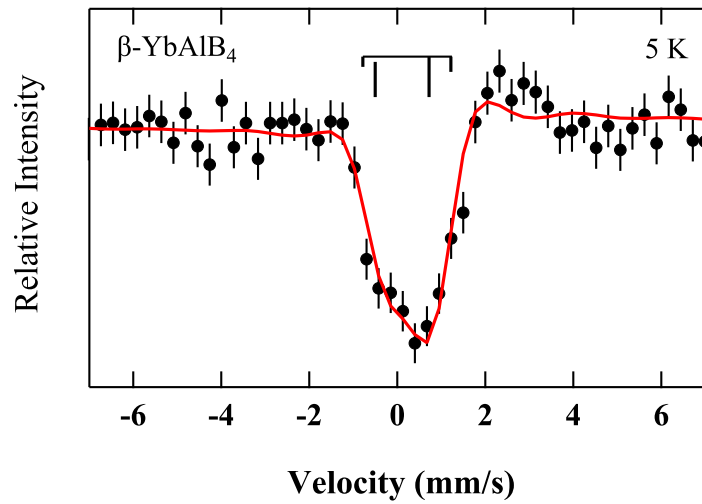


Figure G.8: Synchrotron-radiation-based  $^{174}\text{Yb}$  Mössbauer spectrum of  $\beta\text{-YbAlB}_4$  at 5K. The  $c$ -axis of the single crystalline  $\beta\text{-YbAlB}_4$  samples was tilted though 10 deg from the incident X-ray. The closed circles with error bar indicate the observed spectrum and the red solid line presents the analytical spectrum. The extracted subspectra for two Yb states are shown by the bar-diagrams. The relative intensities of the bar-diagrams represent the evaluated excitation probabilities for the allowed  $^{174}\text{Yb}$  nuclear transitions in the experimental conditions.



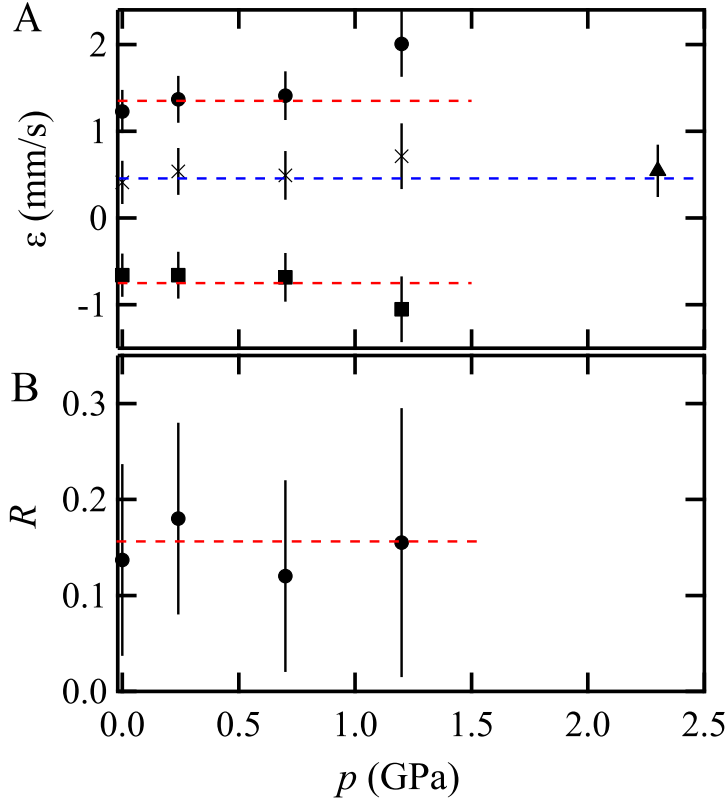


Figure G.9: (A) Refined and evaluated energies  $\varepsilon$  for the nuclear transitions and (B) difference in intensity  $R$  between these two nuclear transitions in  $\beta$ -YbAlB<sub>4</sub> at 2K as functions of pressure. In (A), the solid circles and squares with error bar presents the refined  $\varepsilon$  for two selected  $I_g = 0 \rightarrow I_e^z = \pm 1$  nuclear transitions, respectively, below 1.2GPa. The crosses represent the weighted average  $\varepsilon$  values of two nuclear transitions below 1.2GPa. The solid triangle with error bar indicates the refined  $\varepsilon$  for the single absorption component in the SR-based <sup>174</sup>Yb Mössbauer spectrum of  $\beta$ -YbAlB<sub>4</sub> at 2.3GPa and 2K. The red and blue broken lines are visual guides.

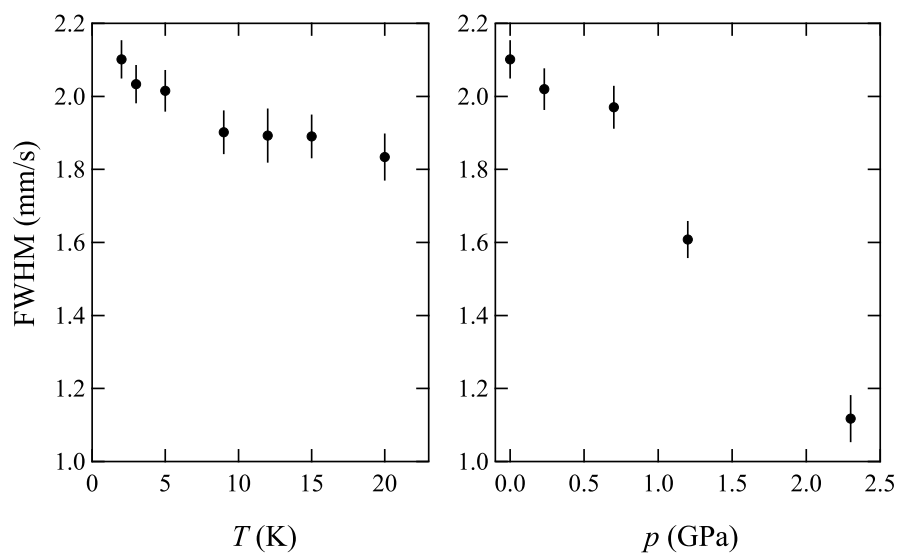
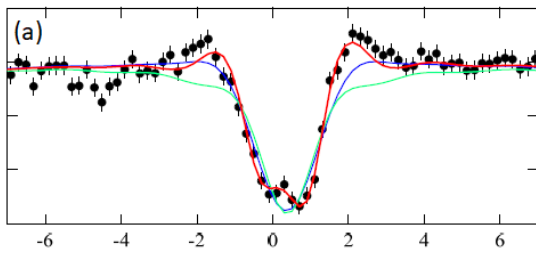


Figure G.10: Evaluated FWHM of the dip in the observed spectra.

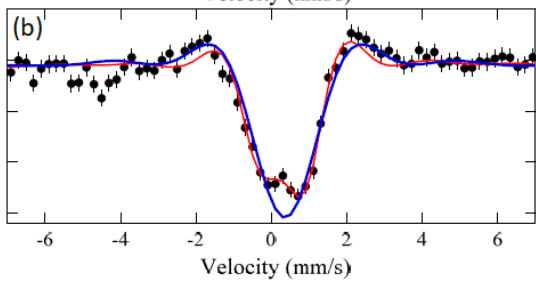
$^{174}\text{Yb}$  SR-based Mossbauer of  $\beta\text{-YbAlB}_4$   
@ 2K & AP



— Analytical result  
— Gaussian  
— Lorentzian

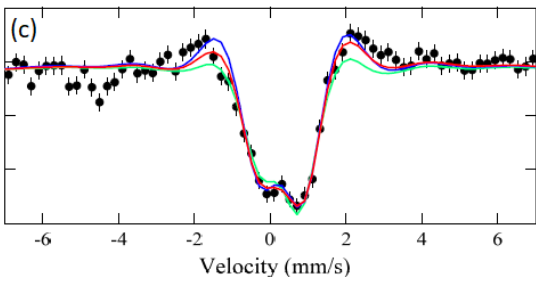
No. of parameters: 3

1 – Gaussian :  $R^2=0.94716$   $\bar{R}^2 = 0.94249$   
1 – Lorentzian :  $R^2=0.85279$   $\bar{R}^2 = 0.83980$



No. of parameters: 3

1 – Gaussian :  $R^2=0.94264$   $\bar{R}^2 = 0.937589$   
1 – Gaussian :  $R^2=0.97020$   $\bar{R}^2 = 0.967098$



No. of parameters: 5

**Analytical :  $R^2=0.98026$   $\bar{R}^2 = 0.97717$**   
2 – Gaussian :  $R^2=0.97090$   $\bar{R}^2 = 0.96635$   
2 – Lorentzian :  $R^2=0.96158$   $\bar{R}^2 = 0.95557$

Figure G.11: Various fits to the experimental lineshape at 2K and ambient pressure.

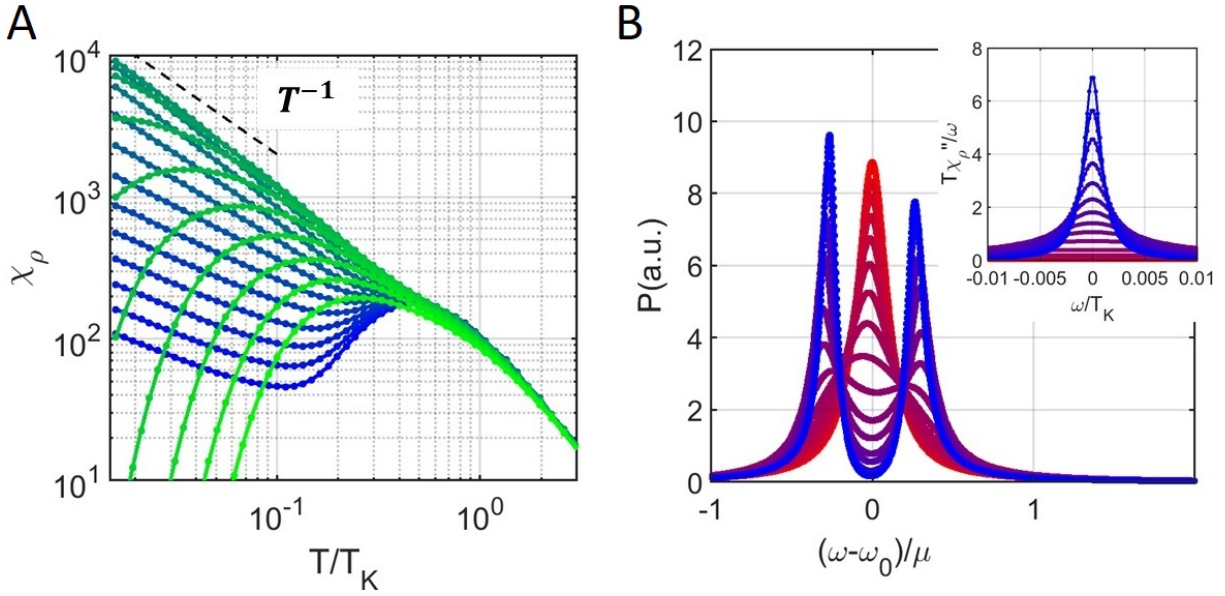


Figure G.12: (A) The static charge susceptibility as a function of  $T$  for various values of  $T_K/J_H$  shows the divergence of the charge susceptibility at the Kondo breakdown QCP between a FL (blue) and a spin-liquid (green). (B) Inset: The dynamical charge susceptibility vs. frequency at the QCP, shows a sharp feature developing as the temperature is lowered from red to blue. Main panel: Consequent splitting of the Mössbauer lineshape at low-temperature as a result of the critical charge fluctuation.

## References and Notes

1. P. W. Anderson, *J. Phys. Soc. Japan* **9**, 316 (1954).
2. R. Kubo, *J. Phys. Soc. Japan* **9**, 935 (1954).
3. M. Blume, J. A. Tjon, *Phys. Rev.* **165**, 446 (1968).
4. M. Blume, *Phys. Rev.* **174**, 351 (1968).
5. Y. Komijani, P. Coleman, *Phys. Rev. B* **94**, 085113 (2016).
6. C. M. Varma, *Rev. Mod. Phys.* **48**, 219 (1976).
7. E. V. Sampathkumaran, *Hyperfine Interactions* **27**, 183 (1986).
8. M. Okawa, *et al.*, *Phys. Rev. Lett.* **104**, 247201 (2010).
9. R. L. Cohen, M. Eibschütz, K. W. West, *Phys. Rev. Lett.* **24**, 383 (1970).
10. I. Nowik, *Hyperfine interactions* **13**, 89 (1983).
11. L. Ruby, S., *J. Phys. Colloques* **35**, C6 (1974).
12. M. Seto, *et al.*, *Phys. Rev. Lett.* **102**, 217602 (2009).
13. R. Masuda, *et al.*, *Appl. Phys. Lett.* **104**, 082411 (2014).
14. G. V. Smirnov, *et al.*, *Phys. Rev. A* **76**, 043811 (2007).
15. F. J. Lynch, R. E. Holland, M. Hamermesh, *Phys. Rev.* **120**, 513 (1960).
16. D. W. Hamill, G. R. Hoy, *Phys. Rev. Lett.* **21**, 724 (1968).
17. M. Seto, *et al.*, *Journal of Physics: Conference Series* **217**, 012002 (2010).

18. R. T. Macaluso, *et al.*, *Chem. Mater.* **19**, 1918 (2007).
19. J. P. Hannon, G. T. Trammell, M. Blume, D. Gibbs, *Phys. Rev. Lett.* **61**, 1245 (1988).
20. Y. H. Matsuda, *et al.*, *Journal of the Korean Physical Society* **62**, 1778 (2013).
21. S. Ofer, I. Nowik, S. G. Cohen, *Chemical Applications of Mössbauer Spectroscopy* (Academic Press, New York, p. 427, 1968).
22. A. J. Freeman, R. E. Watson, *Phys. Rev.* **127**, 2058 (1962).
23. Meyer, C., Gros, Y., Hartmann-Boutron, F., Capponi, J.J., *J. Phys. France* **40**, 403 (1979).
24. Y. Sakaguchi, *et al.*, *J. Phys. Soc. Jpn.* **85**, 023602 (2016).
25. W. Sturhahn, *Journal of Physics: Condensed Matter* **16**, S497 (2004).
26. Y. Matsumoto, *et al.*, *Science* **331**, 316 (2011).
27. T. Tomita, K. Kuga, Y. Uwatoko, P. Coleman, S. Nakatsuji, *Science* **349**, 506 (2015).
28. H. C. Walker, *et al.*, *Phys. Rev. Lett.* **97**, 137203 (2006).
29. K. Hanzawa, T. Kasuya, *Journal of the Physical Society of Japan* **53**, 1809 (1984).
30. H. Winkelmann, *et al.*, *Phys. Rev. Lett.* **81**, 4947 (1998).
31. W. Henning, G. Bahre, P. Kienle, *Zeitschrift für Physik A Hadrons and nuclei* **241**, 138 (1971).
32. M. Ogura, H. Akai, *Journal of Physics: Condensed Matter* **17**, 5741 (2005).
33. H. Akai. Private communication.
34. A. H. Nevidomskyy, P. Coleman, *Phys. Rev. Lett.* **102**, 077202 (2009).

35. Y. Matsumoto, *et al.*, *J. Phys. Soc. Jpn.* **84**, 024710 (2015).
36. A. Ramires, P. Coleman, A. H. Nevidomskyy, A. M. Tsvelik, *Phys. Rev. Lett.* **109**, 176404 (2012).
37. K. Kuga, *et al.*, *Phys. Rev. Lett.* **123**, 036404 (2019).
38. S. Nakatsuji, *et al.*, *Nature Physics* **4**, 603 (2008).
39. A. Legros, *et al.*, *Nature Physics* **15**, 142 (2019).
40. E. C. T. O'Farrell, Y. Matsumoto, S. Nakatsuji, *Physical Review Letters* **109**, 176405 (2012).
41. C. Pépin, *Phys. Rev. Lett.* **98**, 206401 (2007).
42. J. H. Pixley, S. Kirchner, K. Ingersent, Q. Si, *Phys. Rev. Lett.* **109**, 086403 (2012).
43. Y. Komijani, P. Coleman, *Phys. Rev. Lett.* **122**, 217001 (2019).
44. I. G. Lang, Y. A. Firsov, *JETP* **16**, 1301 (1962).
45. D. Sherrington, P. Riseborough, *J. Phys. Colloques* **37**, C4 (1976).
46. A. C. Hewson, D. M. Newns, *Journal of Physics C: Solid State Physics* **12**, 1665 (1979).